https://doi.org/10.1016/j.combustflame.2022.111998

Dimethyl ether oxidation analyzed in a given flow reactor: experimental and modeling uncertainties

Alessandro Stagni[1,*], Steffen Schmitt[2,*], Matteo Pelucchi[1], Alessio Frassoldati[1], Katharina Kohse-Höinghaus[2], Tiziano Faravelli[1]

[1]Department of Chemistry, Materials and Chemical Engineering "G. Natta", Politecnico di Milano, Piazza Leonardo da Vinci 32, 20133, Milano, Italy

[2]Department of Chemistry, Bielefeld University, Universitätsstraße 25, 33615 Bielefeld, Germany

*Corresponding authors; they both contributed equally to this work.

Prof. Alessandro Stagni
Email: alessandro.stagni@polimi.it

Dr. Steffen Schmitt
Email: s.schmitt@uni-bielefeld.de

Supplemental Material:
SM1: Details on experiments and kinetic modeling (.pdf)
SM2: Experimental data (.xlsx)
SM3: Mechanism

Abstract

Dimethyl ether (DME), a widely studied alternative fuel, is known to exhibit complex low- and high-temperature oxidation chemistry. It is also the smallest molecule in the families of symmetric ethers and oxymethylene ethers that receive attention as renewable fuels. Thanks to several studies performed in facilities such as shock tubes, jet-stirred reactors and flames, it can be assumed that the DME oxidation is well understood. However, DME oxidation in flow reactors has been addressed comparatively rarely, although this configuration presents an interesting system with influences of both kinetics and fluid dynamics on the reaction behavior. To examine the interplay of both influences and potential uncertainties resulting from such effects, DME oxidation was experimentally investigated over an extended range of conditions in a flow reactor equipped with mass-spectrometric analysis. Quantitative species profiles were obtained at near-atmospheric pressure in a temperature range of 400–1100 K for three equivalence ratios ϕ (0.8, 1.0 and 1.2), and three flow rates at each stoichiometry. These nine different cases were first analyzed using a detailed chemical reaction mechanism with a Plug-Flow Reactor (PFR) model. In-depth examination of experimental and reaction model uncertainties led to updates in the reaction mechanism that were performed on the basis of most recent, reliable kinetic information. In spite of the good agreement of the PFR model with the experimental data at selected conditions, especially in the low-temperature regime, substantial deviations in the reactivity and associated species profiles were noted in several cases, particularly for lean conditions at low flow rates and intermediate temperatures around and above 700 K. A two-dimensional (2D) computational fluid dynamics (CFD) model was therefore employed to characterize the reactive flow conditions more accurately. Significant contributions of fluid dynamics effects were observed in the cases that presented the most severe deviations, and overall good agreement within experimental uncertainty was obtained for the nine cases with the 2D simulations. With the aid of a mathematical curve matching procedure using a variety of recent, established kinetic mechanisms, it could be convincingly demonstrated under the current conditions that improvements in predictive modeling capability in the sensitive test cases were not a question of improved kinetics but mainly achieved by considering the two-dimensional reactive flow. As a consequence, the present investigation can serve to alert the community to the potential major influences that might be neglected if standard PFR models are used to predict fuel oxidation without detailed analysis whether the conditions are suited to that approach.

Keywords: Dimethyl ether, Plug-flow reactor, Speciation, Modeling, 2D CFD simulation, Uncertainty, Curve matching

1. Introduction

Pursuit of the Sustainable Development Goals [1] with a special focus on climate change mitigation actions [2] calls for scientific and technical advances towards an integrated, non-fossil-based energy system across all sectors including electricity, mobility, heating, chemical and industrial production [3]. While fossil primary energy sources remain dominant, increasing introduction of renewables is anticipated in recent scenarios [4]. Access to renewably produced hydrogen and availability of large-scale energy storage are considered as key elements in the impending transformations [3]. For the transport sector, besides electric driving options, renewable fuels for internal combustion (IC) engines receive increasing attention [5–10], aiming simultaneously for high efficiency, low carbon footprint and reduced local emissions. Many of these alternative fuel compounds are oxygenates, such as alcohols, ethers, esters, ketones and furanics [7–11], that can be produced from (cellulosic) biomass [9–11] or synthesized with available (captured) CO_2 and H_2 from renewable sources [5,6,12,13]. The latter fuel category includes oxymethylene ethers (OMEs) with a molecular formula of $CH_3O(CH_2O)_nCH_3$ that are accessible *via* one- or two-step chemical processes [12–14]. Depending on the specific combustion characteristics, members of this oligomeric ether family offer potential as fuel additives and efficient low-emission drop-in fuels [12–15]. Advantageous features include a low tendency of particulate matter formation owing to the OME structure without carbon-carbon bonds [12] as well as indirect NO_x savings due to higher possible exhaust gas recirculation rates [15]. Complementary recent studies target production, carbon footprint or combustion characteristics of these attractive fuel molecules, including flame and shock tube studies and chemical reaction mechanisms [15,16].

Dimethyl ether (DME) can be regarded as the smallest member of the OME family with n=0. Evaluating different options for electricity-based fuels including methanol, ethanol, butanol, octanol, DME, OME_{3-5} and hydrocarbons with a combined techno-economic analysis, Schemme et al. [5] have recently concluded that the syntheses of methanol and DME have the highest technical maturity, the highest power-to-fuel efficiencies and the lowest manufacturing costs. DME can thus be considered both as the simplest OME fuel and as an attractive target fuel in the energy transformation.

Numerous studies on DME pyrolysis and oxidation have been published during the last two decades. An overview of these experimental and modeling studies as well as their operating conditions (temperature range, equivalence ratios, pressures, and residence times) is provided in Section S.I. in Supplemental Material 1 (SM1). We will point out relevant aspects of the available information here as a background for the present investigation. Despite its apparently simple molecular structure, DME exhibits a complex reaction behavior with low- and high-temperature chemistry [17]. DME ignition is characterized by a

Negative Temperature Coefficient (NTC) at intermediate temperatures. The high-temperature combustion chemistry of DME is relevant for its flame speed and ignition delay times at high temperatures. The low-temperature oxidation of DME, controlling ignition at low temperatures, also received specific attention and many experimental, theoretical and modeling studies are reported [17]. Ignition delay times and flame speeds are fundamental properties of DME/air mixtures and have a direct impact on the design of engines and gas turbines. They are also valuable as benchmarks for DME chemical kinetic mechanism development and validation [18,19].

Ignition delay times of DME were measured using shock tubes and rapid compression machines (RCMs). RCM data mostly focused on low-temperature auto-ignition conditions at high pressures (10–30 bar). Burke et al. [20] studied lean and rich mixtures with air, while Mittal et al. [21] and Shi et al. [22] used N_2 dilution. Shi et al. [22] also studied DME/H_2 mixtures with various hydrogen blending ratios at different pressures and equivalence ratios. Most shock tube studies employed Ar-diluted mixtures and low to intermediate pressures, but Burke et al. [20] and Pfahl et al. [23] measured ignition delays in air at pressures up to 30–40 bar. DME flame speed was measured mostly at ambient conditions of pressure and initial temperature. Only Qin and Ju [24], De Vries et al. [18] and Law and Jomaas, as reported by Zhao et al. [25] performed experiments at pressures up to 10 atm and/or initial temperatures up to 640 K.

Speciation data on the pyrolysis and oxidation of DME were measured in low-pressure premixed flames, flow reactors and jet-stirred reactors (JSRs). These measurements also provide fundamental information for kinetic mechanism development and validation. Dagaut et al. [26,27] studied DME oxidation in a JSR at pressures up to 10 atm. More recently, Le Tan et al. [28], Rodriguez et al. [29], and Moshammer et al. [30] studied DME oxidation at low- and high-temperature conditions in atmospheric-pressure JSRs. Several diagnostics were used by these authors for the quantification of intermediate and final products in DME oxidation.

Alzueta et al. [31] first studied the pyrolysis and oxidation of DME in a laminar flow quartz reactor at atmospheric conditions and temperatures up to 1500 K. Numerous other authors investigated the same fuel using both laminar and turbulent flow reactors, with reactor lengths between 20 and 580 cm, residence times from 0.1 up to 30 s and temperatures below ~1200 K. Most of these studies were performed at ambient or moderate pressures [32]. Curran et al. [33] analyzed DME oxidation in a turbulent flow reactor at low temperatures and in the pressure range of 12–18 atm. More recently, Marrodán et al. [34] and Hashemi et al. [19] investigated DME at high pressures using quartz flow reactors in laminar conditions. Marrodán et al. [34] measured DME oxidation at 450–1050 K and 20–60 bar and focused on its interaction with NO_x. Hashemi et al. [19] studied DME pyrolysis and oxidation at diluted conditions at

50 bar. They also performed experiments on DME/CH_4 mixtures at 100 bar. The same mixture was investigated by Kaczmarek et al. [35] in rich conditions and at low to intermediate temperatures. Porras et al. [36] investigated DME/CH_4 mixtures in a broad range of conditions in different experimental setups (rapid compression machine, shock tube, and flow reactor). Zheng et al. [37] and Jiang et al. [38] employed a counterflow configuration to study ignition and extinction behavior of laminar diffusion and partially-premixed DME flames. Reuter et al. [39] investigated the ozone-assisted cool flames of DME in a counterflow burner and examined the uncertainties of reactions contributing significantly to the low-temperature heat release. They concluded that their kinetic model, which incorporated rates from the mechanisms of Burke et al. [20], Curran et al. [40], Fischer et al. [41], Dames et al. [42], Wang et al. [43] and Zhao et al. [25], significantly overpredicted the cool flame extinction limits.

Complementary to the available experimental information, modeling of the DME pyrolysis and oxidation chemistry can also be regarded as quite advanced. The development of kinetic mechanisms for DME started about 25 years ago, with the mechanisms of Dagaut and coworkers [26,27] and Curran and coworkers [33,40,41]. Alzueta et al. [31] developed a model for DME/NO_x interactions combining the Curran et al. mechanism [40] with the NO_x sub-mechanism from Glarborg et al. [44]. They added NO_x–DME interaction reactions and also modified some DME reactions, namely H-abstraction reactions and the reactions of CH_3OCH_2+O_2. Zhao et al. [25] developed a new mechanism in 2008, which incorporated several developments in small species kinetics and thermochemistry updates and implemented the low-temperature reaction subset from Curran et al. [33] to yield a comprehensive model for DME combustion. The model of Zhao [25] was later adopted and modified in numerous studies, such as Liu et al. [45], Herrmann et al. [46], Kurimoto et al. [47] and Prince and Williams [48].

Three new mechanisms were independently developed in 2015, *i.e.*, the mechanisms of Burke et al. [20], Rodriguez et al. [29] and Wang et al. [43]. The mechanism of Burke et al. [20] was the first one to incorporate high-level rate constant measurements and calculations for the reactions of DME. Also, they applied a pressure-dependent treatment to the low-temperature reactions of DME. Rodriguez et al. [29] showed that the models of Zhao et al. [25] and Burke et al. [20] overestimated DME reactivity in the low-temperature region. They thus developed a new detailed kinetic mechanism based on a theoretical investigation of the reactions involving CH_3OCH_2OO and derived radicals; they validated it using mainly data obtained for low-temperature oxidation and ignition, but also included a few tests for pyrolysis and flame conditions. The kinetic parameters used in this mechanism [29] for DME were taken from the literature or evaluated using quantum calculations. Wang et al. [43] studied DME oxidation in a laminar flow reactor and developed a new kinetic mechanism to reduce the gap between model predictions and

experimental results for key oxygenated species and fuel conversion. The kinetic mechanism, developed from the widely used one of Zhao et al. [25], focused on the low-temperature oxidation reactivity by including an additional, chemically-activated pathway of the CH_3OCH_2 reaction with O_2, as well as new decomposition chemistry of OCH_2OCHO radical, investigated theoretically in their work [43].

The subsequently published mechanism of Dames et al. [42] is based on the Burke et al. [20] mechanism, recognizing that it was found superior to model low-temperature conditions compared to the mechanism of Rodriguez et al. [29] and the low-temperature chemistry set of Eskola et al. [49]. A number of advances in DME combustion were included in this mechanism [42], namely a re-evaluation of the termination reaction $2CH_3OCH_2OO=O_2$+products and accurate computation of pressure-dependent unimolecular decomposition rates for several radical intermediates of DME. Reuter et al. [39] updated the Princeton kinetic mechanism, which then incorporated rates from the mechanisms of Burke et al. [20], Curran et al. [40], Fischer et al. [41], Dames et al. [42], Wang et al. [43] and Zhao et al. [25]. They modified the rates of H-abstraction reactions on DME, and of the decomposition of $CH_2OCH_2O_2H$ (QOOH) and HO_2CH_2OCHO (hydroperoxymethyl formate).

The most recent mechanisms are from Hashemi et al. [19] and Shrestha et al. [50]. The former developed a mechanism for DME and CH_4/DME combustion at high pressure (up to 100 bar). In their work [19], the authors evaluated DME reactions one-by-one and adopted the most reliable rate constants from different sources without any tuning. Regarding the low-temperature chemistry, the main sources in this mechanism [19] are the mechanisms of Burke et al. [20], Dames et al. [42] and the theoretical work of Eskola et al. [49]. Shrestha et al. [50] developed a kinetic mechanism for the DME/DMM/NO_x system. The elementary reactions in their DME sub-mechanism were compiled from several contributions, and in particular the low-temperature chemistry is mostly based on the schemes of Burke et al. [20] and Wang et al. [43].

In spite of this suite of work, uncertainties in DME oxidation kinetics still exist, and they are primarily associated to the low-temperature chemistry, in particular to the first and second O_2 additions to DME radicals and the decomposition pathways and/or the branching ratio of the keto-hydroperoxide species [17,42,47,51]. Tomlin et al. [52] highlighted the need for further work in this area, since several kinetic models [37,45,53] failed to accurately predict DME autoignition in RCM conditions. In particular, they highlighted the need for accurate pressure-dependent descriptions of O_2 additions to DME radicals and subsequent pathways forming OH [52]. Several studies investigated DME low-temperature chemistry and theoretically evaluated these reactions using *ab initio* methods [20,49]. However, Hashemi et al. [19] recently pointed out that further work is still needed to reconcile experimental and theoretical work on

reactions on the CH_3OCH_2OO potential energy surface (PES) with ignition delay measurements in the NTC region for DME.

Recognizing this level of understanding, we revisit the analysis of DME oxidation in the present work with a focus on a given plug-flow reactor (PFR) configuration. It permits access to the low- to intermediate-temperature regime of interest and covers the ignition and main fuel conversion regions, where the former is accessible for experimental investigation in JSRs, but not in flames: as a matter of fact, investigating DME behavior in such conditions becomes of particular relevance in engines, as ignition dynamics affects their whole operation and efficiency. Moreover, in contrast to JSRs, PFRs offer the investigation of both fluid dynamic and kinetic effects. Also, similar to shock tubes, but different from JSRs, the PFR configuration separates reactants and products, permitting detailed kinetic analyses along the reaction progress. Advantageously, multiple chemical species profiles can be obtained as a function of reaction conditions, while such information is rarely available in shock tubes or RCMs. The PFR can thus be regarded as a valuable test case permitting insight into the coupling of chemistry and fluid dynamics for some relevant conditions in temperature, pressure and stoichiometry space.

Turbulent and laminar flow reactors were widely used to study pyrolysis and oxidation of DME. Referring to the experimental studies mentioned in Table S1 in SM1, turbulent flow reactors were utilized by Curran et al. [33] (*Re* numbers of ≈10,000), Fischer et al. [41] (*Re* of ≈7,000) and Schönborn et al. [32] (*Re* of ≈20,000). All remaining experiments in Table S1 were performed using laminar flow reactors with *Re* numbers ranging between 10 and 1000, reactor diameters of 0.5 to 2.37 cm and reactor lengths of 20 to 580 cm (average size ≈1 m). Most of the reactors are in quartz, but some of them are made with stainless steel or silica.

Due to the large differences in laminar flow reactors design, size and flow conditions, it is important to evaluate the assumption of plug flow in modeling these experiments. We are following up on previous work, including that of Dryer et al. [54] who discussed the plug-flow assumption and concluded that it is frequently applied without a careful vetting of potential sources of departure from this behavior. Wada et al. [55] studied the impact of two-dimensional (2D) *vs.* PFR assumptions for the first-stage ignition delay time of DME/air mixtures in the low-temperature regime. Their analysis showed that assuming a plug-flow model leads to a large overprediction of the first-stage ignition delay times at low temperatures. Their work referred to a long reactor (*L*=580 cm), with a diameter *D*=2 cm, and a Reynolds number *Re*=1250. Guo et al. [56] experimentally investigated the low-temperature oxidation of DME with a laminar flow reactor (*L*=35.5 cm, *D*=1.7 cm, *Re*≈10). Dryer et al. [54] presented a detailed analysis of this experiment using a 2D model based on OpenFOAM®. Their analysis revealed the presence of clear axial and radial

gradients in temperature and species concentration. In some conditions, these gradients were large enough to support significant local axial diffusion, which invalidates a plug-flow assumption. Results showed that the two-dimensional interpretation of the flow tube experiments substantially affected the predicted species fractions at the reactor exit; assuming a plug-flow model resulted in a delay in the low-temperature reactivity of ≈25 K [54]. Kurimoto et al. [47] also compared PFR and 2D modeling of DME oxidation in a laminar flow reactor (L=35.5 cm, D=1.7 cm, Re≈10), but differently from the previous investigation, they found that the PFR modeling assumption resulted in an over-prediction of DME fuel consumption by 22%.

To analyze such potential influences in more detail, we provide a combined experimental and modeling analysis of DME oxidation in the present work. We use mass-spectrometric analysis of the reactions of DME/O_2/Ar mixtures in a PFR (L=130 cm, D=0.726 cm, Re≈20–130) in the temperature range of 400–1100 K at 970 mbar at three different equivalence ratios ϕ (0.8, 1.0, and 1.2) for three different flow rates at each stoichiometry, thus providing a set of quantitative species-temperature profiles at nine different combinations of equivalence ratio and total flow rate. At the same time, we perform a wide-range uncertainty analysis, considering the several different sources for data variability. This is essential to interpret such results through kinetic and fluid-dynamic modeling, as well as to quantify the modeling accuracy. Indeed, such an attention to uncertainties is not common in most of scientific works concerning combustion experiments in ideal reactors; here, we provide a systematic discussion to frame it in a quantitative fashion. These nine cases are modeled with both PFR and 2D simulations to provide information on the impact of fluid dynamics. The chemical mechanism in both the low- and intermediate-temperature regions is inspected to provide most recent, consistent kinetic and thermodynamic information and analyzed regarding potential further improvements. This is leveraged to interpret the experimental results, perform kinetic analysis and understand the governing pathways. A thorough analysis of experimental and modeling uncertainties is performed as a basis for reliable predictions and is thought to provide guidance for similar assessments regarding further alternative fuel targets such as those of the OME family.

2. Experimental approach

All experiments were performed in a plug-flow reactor at Bielefeld University. The system has been previously described in detail [57,58] with some optimizations explained in [59]. A scheme of the PFR can be found in Fig. S1 in SM1. The reactor itself consists of a cylindric, fused silica tube (L=130 cm, D=0.726 cm) with flat inner and outer walls that can be heated to up to 1200 K by a surrounding ceramic oven. The

temperature profile along the reactor length can be described by an empiric approach that is explained in Section S.II. in SM1. All gases (Linde AG, purity ≥99.5%) are supplied through a preheated (423 K) mixing line by mass flow controllers (MKS Instruments, 5% uncertainty). After passing the reactor tube, species are continuously sampled using a rapid two-stage expansion (1st stage ≈10^{-4} mbar, 2nd stage ≈10^{-6} mbar) and analyzed by a time-of-flight mass spectrometer ($m/\Delta m$≈2500, ionization energy 20 eV). The sampling nozzle (quartz, ~150 µm opening diameter) is located in the fused silica tube behind the ceramic oven. This construction enables the formation of a molecular beam which freezes further reactions. Therefore, the species composition in the mass spectra can be considered to be the same as at the nozzle tip inside the reactor. Temperature-dependent measurements were performed by decreasing the reactor temperature with a constant ramp speed of 33 s/K at a constant reactor pressure of 970 mbar. Table 1 summarizes these experimental parameters.

Table 1: Experimental parameters for the plug-flow reactor experiments.

Parameter	Value
Reactor pressure p	970 mbar
Reactor length L	130 cm
Reactor diameter D	7.26 mm
Total flow rates f	250, 500, 750 sccm
Residences times τ	1.1 to 6.9 s

The investigated conditions are summarized in Table 2. A combination of three different equivalence ratios ϕ (0.8, 1.0 and 1.2) and three different total flow rates f (250 sccm, 500 sccm and 750 sccm) was chosen to study DME combustion and possible influences of fluid dynamics systematically under a wide range of conditions. Since the total flow rate was kept constant during one measurement, residence times τ are dependent on the reactor temperature and vary between 1.1 and 6.9 s for the aforementioned conditions. This dependence is displayed in Fig. S3 in SM1 and approximated by the equations given in the last column of Table 2. Since only 3% of the gas mixture is reactive and the reactors' heat capacity is large in relation to the heat formed due to exothermal reactions, the temperature increase caused by these reactions is expected to be small (< 5 K).

Table 2: Experimental conditions for the plug-flow reactor experiments.

Case	Equivalence ratio ϕ	Argon dilution	Flow rates (sccm)				τ* / s
			Total	Ar	DME	O_2	
01	0.80	97%	250.50	243	1.579	5.92	3169/*T*[K]
02	1.00	97%	250.51	243	1.875	5.63	3169/*T*[K]
03	1.20	97%	250.50	243	2.143	5.36	3169/*T*[K]
04	0.80	97%	500.00	485	3.158	11.84	1586/*T*[K]
05	1.00	97%	500.00	485	3.750	11.25	1586/*T*[K]
06	1.20	97%	500.00	485	4.286	10.71	1586/*T*[K]
07	0.80	97%	750.50	728	4.737	17.76	1058/*T*[K]
08	1.00	97%	750.51	728	5.625	16.88	1058/*T*[K]
09	1.20	97%	750.50	728	6.429	16.07	1058/*T*[K]

*This calculation is based on PFR simulations using the PFR model described in Section 3.2.1.

The data evaluation was described in detail previously [60,61] and is therefore only briefly summarized here. The fundamental correlation used to convert the mass spectrometer signal intensities S_i of a species i into the corresponding mole fraction x_i is given by Eq. (1) [60]:

$$\frac{S_i}{S_{\mathrm{Ar}}} = \frac{x_i}{x_{\mathrm{Ar}}} \cdot k_{i/\mathrm{Ar}}(E) \qquad (1).$$

The non-reactive dilution gas argon is used as a reference species here. Energy- and species-dependent calibration factors $k_{i/\mathrm{Ar}}(E)$ were calculated based on an elemental balance approach for all major species, *i.e.*, reactants, products and argon [60]. Intermediate species were quantified by simulating signal intensities using a convolution method [60], which requires electron ionization (EI) cross-section data from the literature for the respective species. These details of the quantification process are summarized in Table S2 in SM1. All experimental data is available in Supplemental Material 2 (SM2).

2.1 Measurement uncertainty and errors

Considering the experimental uncertainties and understanding their origin is a prerequisite to reliably analyze experimental data and convincingly compare them with simulation results. Therefore, we chose to devote this section to comprehensively discuss this topic which often does not get the necessary attention. An overview of error sources regarding the present experiments is given in Table 3.

Global signal fluctuations that, e.g., originate from electronic noise do not influence the quantified data due to normalizing all signals to the Ar signal. However, individual signal fluctuations like signal noise can

influence the resulting mole fractions. This effect varies from ≈1% for major species with a high signal intensity to up to 10% for intermediates with a low signal intensity. This effect can be larger for species near the detection limit (mole fraction $\approx 10^{-6}$) which were, however, not detected in this work. Rest gas in the reactor and mass spectrometer mainly consists of water, nitrogen and oxygen and therefore impacts these species' signals and the CO signal due to the small mass difference between CO and N_2. This effect can be reduced by applying a background correction. Impurities in the used chemicals are considered to have a very minor influence due to their high purities of at least 99.5%. The inlet gas composition and therefore the chosen equivalence ratio can be altered by about ±5% considering the uncertainty of the used mass flow controllers. Reactor pressure fluctuations of up to ±5 mbar can be observed during a measurement which should not largely influence the experimental results since the pressure dependence of most reactions is not changing strongly at 970 mbar. While the Ni-Cr/Ni thermocouples used to control the reactor temperature usually have an uncertainty of ±1 K, it must be considered that these thermocouples are placed on the ceramic oven and not inside the reactor tube itself. This results in a higher uncertainty of about ±15 K for the reactor temperature. A temperature dependence of the calibration factor for oxygen was noted previously [61], the origin of which remained unclear. Here we would like to point out that the mole fraction of oxygen should be considered to have a higher uncertainty at high temperatures regarding the previous observation. The quantification process itself leads to an uncertainty of about ±10% when using an elemental balance approach as it was done for major species in this work. When using the convolution procedure described in [60] to quantify intermediates, the experimental uncertainty mainly depends on the quality of the respective EI cross sections available in the literature.

In general, these factors result in an uncertainty of about ±20% for most major species and a factor of 2 for the intermediates observed in this work. Since some aspects only have an individual influence on some species, the estimated species-dependent uncertainties are summarized in Table S2 in SM1 and the resulting uncertainty bands are displayed as shaded areas in all figures containing experimental data. This visualization of the uncertainty allows for a meaningful comparison with modeling results.

Table 3: Summary of sources for the experimental uncertainties and their respective influence on the results.

Source	**Affected species**	**Estimated uncertainty caused by the phenomena**
Global signal fluctuations	All	None, due to the Ar normalization
Individual signal fluctuations	All	Between ≈1% and ≈10% depending on the species' signal intensity

Rest gas within reactor	H_2O, CO, O_2	Depending on background/species signal ratio
Temperature control	All	±15 K
Pressure control	All	±5%
Mass flow controllers	All	±5% (total uncertainty of all inlet gases combined)
T-dependent calibration	O_2	Leads to higher uncertainty of O_2 at higher *T*
Elemental balance, direct calibration	Major species	±10%
Signal convolution	Intermediates	Factor between 2 and 4 depending on the quality of available literature data on ionization properties

3. Modeling

3.1. Kinetic mechanism

The CRECK kinetic mechanism for DME pyrolysis and oxidation includes 126 chemical species and 2111 reactions and is attached as Supplementary Material 3 (SM3) to this work. Built up according to the hierarchy and generality principles, it implements the Aramco2.0 mechanism for C_0–C_2 species by Kéromnès et al. [62] and Metcalfe et al. [53], updated as reported in Bagheri et al. [63]. C_3 and higher-molecular-weight species are from Burke et al. [20] and Ranzi et al. [64]. The DME kinetic subset, including thermodynamic and transport properties, is mostly from Burke et al. [20], and it accounts for 14 chemical species and 56 chemical reactions.

Moving from the accurate speciation measurements and kinetic analysis for pure DME oxidation by Wang et al. [43] and Moshammer et al. [17,30], as well as from the successful implementation of the Korcek mechanism [65] in the low-temperature oxidation of alkanes [66], additional reaction pathways were implemented so as to better predict the formation and consumption of measured intermediate species such as carbonic (HOCOOH) and formic (HOCHO) acids. While a kinetic subset managing formic acid is already contained in the core mechanism, a new decomposition and oxidation reaction subset was introduced for carbonic acid based on analogy with the recent theoretical and kinetic modelling study on acetic acid by Cavallotti et al. [67].

A schematic of the main oxidation pathways of DME is provided in Fig. 1, highlighting (in red) the new pathways added in the present study.

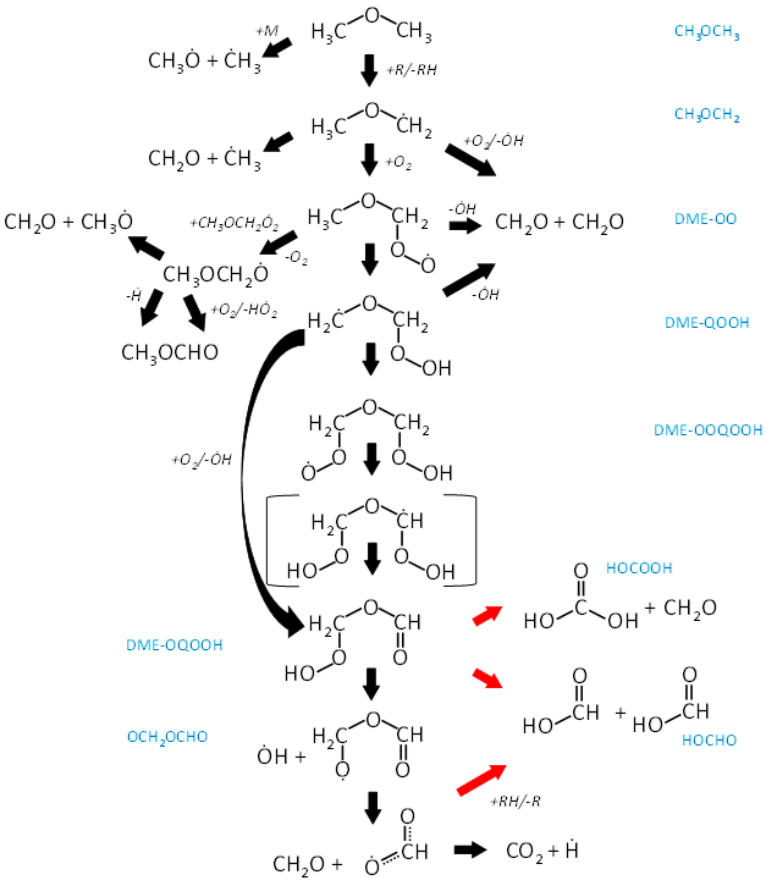

Figure 1: Main oxidation pathways of DME at low, intermediate and high temperature. Pathways added in the present mechanism are highlighted in red. Species names in the kinetic model are given in blue.

As mentioned above, most of the reaction pathways and kinetic parameters for DME oxidation have been adopted from Burke et al. [20], and the reader is referred to this previous study for related sources of model parameters. H-abstraction reactions by H, OH, HO_2, $O(^3P)$ and CH_3 have been updated based on the recent theoretical study by Cavallotti et al. [68]. The pre-exponential factor of the H-abstraction by HO_2 has been increased of a factor of 2 for better agreement with DME experimental targets across the intermediate-temperature range where an NTC behavior is observed for DME. Detailed references of the source of the remaining kinetic rate coefficients updated with respect to Burke et al. [20] are given in Table 4.

Table 4: Rate coefficients for DME oxidation that have been changed or added compared to Burke et al. [20] in this study and their literature source. Units are cm^3, mol, cal, s. For pressure-dependent reactions, only high-pressure limit (HPL) rate parameters are reported.

Reaction	Rate coefficient (HPL)			Ref.	Notes
	A	***n***	***Ea***		
$CH_3OCH_3+H=H_2+CH_3OCH_2$	$4.73\cdot10^4$	2.84	3405.52	[68]	
$CH_3OCH_3+OH=H_2O+CH_3OCH_2$	$2.19\cdot10^7$	1.91	-374.33	[68]	
$CH_3OCH_3+HO_2=H_2O_2+CH_3OCH_2$	$2.09\cdot10^2$	3.34	13906.37	[68]	Ax2
$CH_3OCH_3+CH_3=CH_4+CH_3OCH_2$	$3.85\cdot10^{-2}$	4.39	6435.80	[68]	
$CH_3OCH_3+O=OH+CH_3OCH_2$	$7.28\cdot10^7$	1.86	3533.45	[68]	
DME-OQOOH=OCH_2OCHO+OH	$2.00\cdot10^{16}$	0.00	40500.00	[25]	
DME-OQOOH=HOCOOH+CH_2O	$1.50\cdot10^2$	2.13	27500.00	[66]	
DME-OQOOH=HOCHO+HOCHO	$1.50\cdot10^2$	2.13	27500.00	[66]	

At high temperatures (*T*>1200 K), the unimolecular reaction forming methyl (CH_3) and methoxy radical (CH_3O) initiates the radical chain mechanism. H-abstraction reactions by different radicals (e.g., H, OH, CH_3, HO_2, $O(^3P)$) lead to the formation of the CH_3OCH_2 radical, that decomposes through β-scission producing formaldehyde (CH_2O) and CH_3. At low temperatures, DME oxidation follows similar pathways to those largely established for *n*-alkanes [69,70]. The low-temperature branching pathway starts with a first addition to oxygen (O_2) by the fuel radical CH_3OCH_2, forming the alkyl-peroxy radical (DME-OO). A chemically activated reaction with O_2 competes with the first addition reaction, forming OH and two formaldehyde molecules. DME-OO can isomerize via a 6-membered ring transition state to form hydroperoxyl alkyl radical (DME-QOOH), or decompose through β-scission, also forming two molecules of formaldehyde and OH. The second addition to O_2 produces the peroxy-hydroperoxyl-alkyl radical (DME-OOQOOH) that further isomerizes and rapidly decomposes to form the carbonylhydroperoxide hydroperoxymethyl formate (DME-OQOOH). This latter molecule can decompose *via* a unimolecular reaction producing OH and the alkoxy radical OCH_2OCHO, globally leading to formaldehyde, CO_2 and Ḣ, thus providing chain branching. Alternatively, the Korcek mechanism produces stable products such as carbonic acid (HOCOOH) and formaldehyde, or formic acid (HOCHO).

Moshammer and co-workers [17] highlighted the formation of methyl formate (CH_3OCHO) during the lean (*i.e.*, ϕ=0.35) low-temperature (*T*=500–700 K) oxidation of DME in 78% argon in a jet-stirred reactor. Methyl formate can be formed by the recombination/disproportionation reaction of DME peroxy radical (DME-OO) yielding O_2 and CH_3OCH_2O, that can decompose through β-scission reactions forming methoxy radical and formaldehyde or Ḣ and methyl formate at high temperatures. At lower temperatures, H-abstraction by O_2 on CH_3OCH_2O directly forms CH_3OCHO and HO_2. The performic (HO_2CHO) and carbonic

(HOCOOH) acid isomers were also measured in that work [17] in non-negligible quantities. Performic acid is formed by the H-abstraction reaction on the carbon site carrying the hydroperoxy substitution of DME carbonylhydroperoxide (DME-OQOOH) followed by the β-scission of the radical forming performic acid and HCO. A competing β-scission reaction breaking the O-O bond of the hydroperoxy substitution can lead to the formation of formic anhydride and OH. None of these pathways, whose rate coefficients were based on analogy with the new reaction classes introduced in alkane low-temperature oxidation by Ranzi et al. [66], were found to be effective here. Further investigations are needed to reconcile theory and the experimental observation found in [17,30,43]. As mentioned above, the Korcek mechanism was accounted for in the revised model and partly justifies the formation of carbonic acid and formaldehyde or, alternatively, two formic acid molecules as depicted in Figure 1.

3.2 Flow reactor models

In order to interpret the experimental results, and to gain a fundamental insight on the chemistry–fluid dynamic interactions in the flow reactor, the experimental facility was represented through two different degrees of complexity: i) a plug-flow, perfectly segregated model, and ii) a two-dimensional, laminar computational fluid dynamics (CFD) solver. The suitability of the plug-flow assumption was first assessed through an *a priori* analysis, *i.e.*, through the evaluation of the Peclet (*Pe*) number, which is usually the main criterion to assess the plug-flow assumption; indeed, this compares the importance of transport by advection to transport by diffusion. Values of the critical dimensionless numbers, including Reynolds (*Re*) and Prandtl (*Pr*) numbers, are shown in Fig. 2 for all conditions explored in this work. For the sake of simplicity, the evaluation of both *Re* and *Pr* was performed by using a non-reactive 100% Ar mixture.

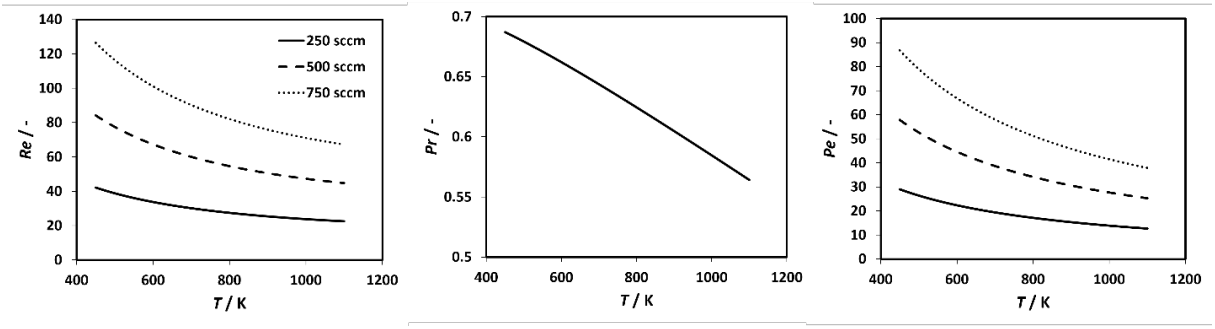

Figure 2: Dimensionless numbers (*Re*, *Pr*, *Pe*) for the different conditions of the flow reactor.

For all considered conditions, it can be noticed that $Pe \gg 1$, thus axial diffusion can be considered as negligible, if compared to advection. According to the Levenspiel diagram [71], and supposing a comparable behavior of Prandtl and Schmidt (Sc) numbers, the flow is in the axial dispersion regime. However, a more comprehensive evaluation of the role of diffusion and conduction, both radial and axial,

was performed *via* direct comparison of the plug-flow and 2D model. Their respective governing equations are summarized in Sections 3.2.1 and 3.2.2.

3.2.1 Plug-flow reactor

The steady-state equations governing the plug-flow model, with a prescribed temperature profile, are reported below under the form of an ordinary differential equation (ODE) system. A temperature profile was prescribed to the flow reactor, following the correlation illustrated in Section S.II. in SM1, *i.e.*, not solving the energy balance. Thus, the equations constituting the model are only related to the mass balance and to the residence time reconstruction, respectively:

$$\rho v \frac{\mathrm{d}Y_i}{\mathrm{d}\xi} = W_\mathrm{i}\dot{\omega}_\mathrm{i} \qquad i=1\ldots N_\mathrm{S} \tag{2}$$

$$\frac{\mathrm{d}\tau}{\mathrm{d}\xi} = \frac{1}{v} \tag{3}$$

where ρ is the density, v is the velocity, Y_i is the mass fraction of the *i*-th species, ξ is the spatial coordinate, W_i is the molecular weight of the *i*-th species, $\dot{\omega}_i$ is its formation rate and τ the residence time. The related solver belonging to the `OpenSMOKE++` suite [72] is adopted to this purpose.

3.2.2 2D laminar model

The 2D laminar model solves the conservation equations for mass, momentum, species and energy. A continuous, compressible, multicomponent gas-phase mixture is considered, and body forces are neglected. The respective equations are listed below:

$$\frac{\partial \rho}{\partial t} + \nabla\cdot(\rho \boldsymbol{v}) = 0 \tag{4}$$

$$\frac{\partial}{\partial t}(\rho \boldsymbol{v}) + \nabla(\rho \boldsymbol{v}\boldsymbol{v} + P\boldsymbol{I}) = \nabla\tau \tag{5}$$

$$\frac{\partial}{\partial t}(\rho Y_i) + \nabla\cdot(\rho Y_i \boldsymbol{v}) = -\nabla\cdot\left(\rho Y_i \boldsymbol{V_i^C}\right) + \dot{\omega}_\mathrm{i} \qquad \mathrm{i}=1\ldots N_\mathrm{S} \tag{6}$$

$$\rho c_p \frac{\partial T}{\partial t} + \rho c_p \boldsymbol{v}\cdot\nabla T = -\nabla\cdot\boldsymbol{q} - \rho\nabla T\cdot\sum_{\mathrm{i}=1}^{NS} c_{p,i} Y_i \boldsymbol{V_i^C} - \sum_{\mathrm{i}=1}^{NS} h_\mathrm{i}\dot{\omega}_\mathrm{i} \tag{7}$$

where t is the time, v is the velocity vector, P is the pressure, $\boldsymbol{V_i^C}$ is the corrected diffusion velocity [73] of the *i*-th species, c_p and $c_{p,\mathrm{i}}$ are the constant-pressure specific heat capacities of the mixture and of the *i*-th species, respectively, T is the temperature, h_i is the specific enthalpy of the *i*-th species, and $\boldsymbol{q}$ is the heat flux vector, considering only the conduction contribution:

$$\boldsymbol{q} = -\lambda\nabla T \tag{8}$$

Due to cylindrical symmetry, only a small slice is simulated, such that the case can be considered as two-dimensional. The simulation was performed *via* the `laminarSMOKE` solver [74]. This tool was specifically targeted at modeling laminar reactive flows using detailed kinetic mechanisms. It is based on the `OpenFOAM®` framework, specifically the `pisoFOAM` solver for compressible, unsteady, non-reacting flows, adapted to manage reacting flows and detailed kinetic mechanisms. Boundary conditions are summarized in Table 5.

Table 5. Boundary conditions used for the CFD simulations.

Boundary	Velocity	Pressure	Temperature	Species
Inlet	$v = v_{inlet}$	Zero Gradient	$T = T_{inlet}$	DME/O_2/Ar
Wall	No-slip	Zero Gradient	$T_{profile}$	Zero Gradient
Outlet	Inlet/Outlet	p = 970 mbar	Zero Gradient	Zero Gradient

To enhance convergence, the resolution strategy involved the use of 2 meshes with a different resolution: i) a coarse mesh (460 cells), and ii) a refined one (27600 cells). With a progressive approach, convergence was attained in three steps:

1) Simulation of the coarse mesh through the unsteady `laminarPimpleSMOKE` solver, for an overall time length of 10 s, *i.e.,* sufficiently larger than the maximum residence time (≈7 s).
2) Simulation of the refined mesh through the unsteady `laminarPimpleSMOKE` solver, using the results obtained at the point 1) as the starting point. The simulation was stopped when the residuals of the equations involving temperature, velocity and major species reached an asymptotic behavior.
3) Simulation of the refined mesh through the stationary `laminarSimpleSMOKE` solver, using the results obtained at the point 2) as the first guess. Here, too, the simulation was stopped when the residuals of the mentioned equations reached an asymptotic behavior and were sufficiently low (*i.e.*, below $1 \cdot 10^{-6}$).

For each step, 4 cores (Intel® Xeon® CPU E5-2630 v3 @ 2.40 GHz) were used on a parallel cluster. On average, ≈3 days were required for step 1), ≈10 days for step 2) and ≈7 days for step 3). Higher-temperature cases were more time-consuming, due to the heavier weight of the chemical time step.

4 Results

In the following, Section 4.1 presents results from the experiments and simulations with both, PFR and 2D modeling approaches for the investigated broad range of conditions, including an analysis of the fluid dynamics and 2D effects. In Section 4.2, the influences of the kinetic mechanism, remaining uncertainties

and further possible improvements are discussed. Finally, the model performance is analyzed in Section 4.3 considering both, kinetics and fluid dynamic influences including comparison with other established reaction mechanisms through a curve matching approach.

4.1 Comparison of experimental data and simulation results

Figure 3 shows the effect of equivalence ratio and flow rate (*i.e.*, residence time) on the conversion of DME in the laminar flow reactor. For all investigated conditions, a low-temperature reactivity is visible between 500 and 600 K, followed by the NTC region. Finally, the complete oxidation of DME takes place at higher temperatures. The measurements show that the low-temperature reactivity is relatively insensitive to the different operating conditions investigated in this work in terms of equivalence ratio and residence time. On the contrary, the high-temperature oxidation is largely affected by the variation of the residence time. Complete conversion of DME can be observed at ≈850 K for the long residence time (cases 01–03, $\tau \approx 3.7$ s), while a higher temperature of ≈950 K is needed for the short residence time (cases 07–09, $\tau \approx 1.1$ s). The effect of equivalence ratio on the reactivity is less important.

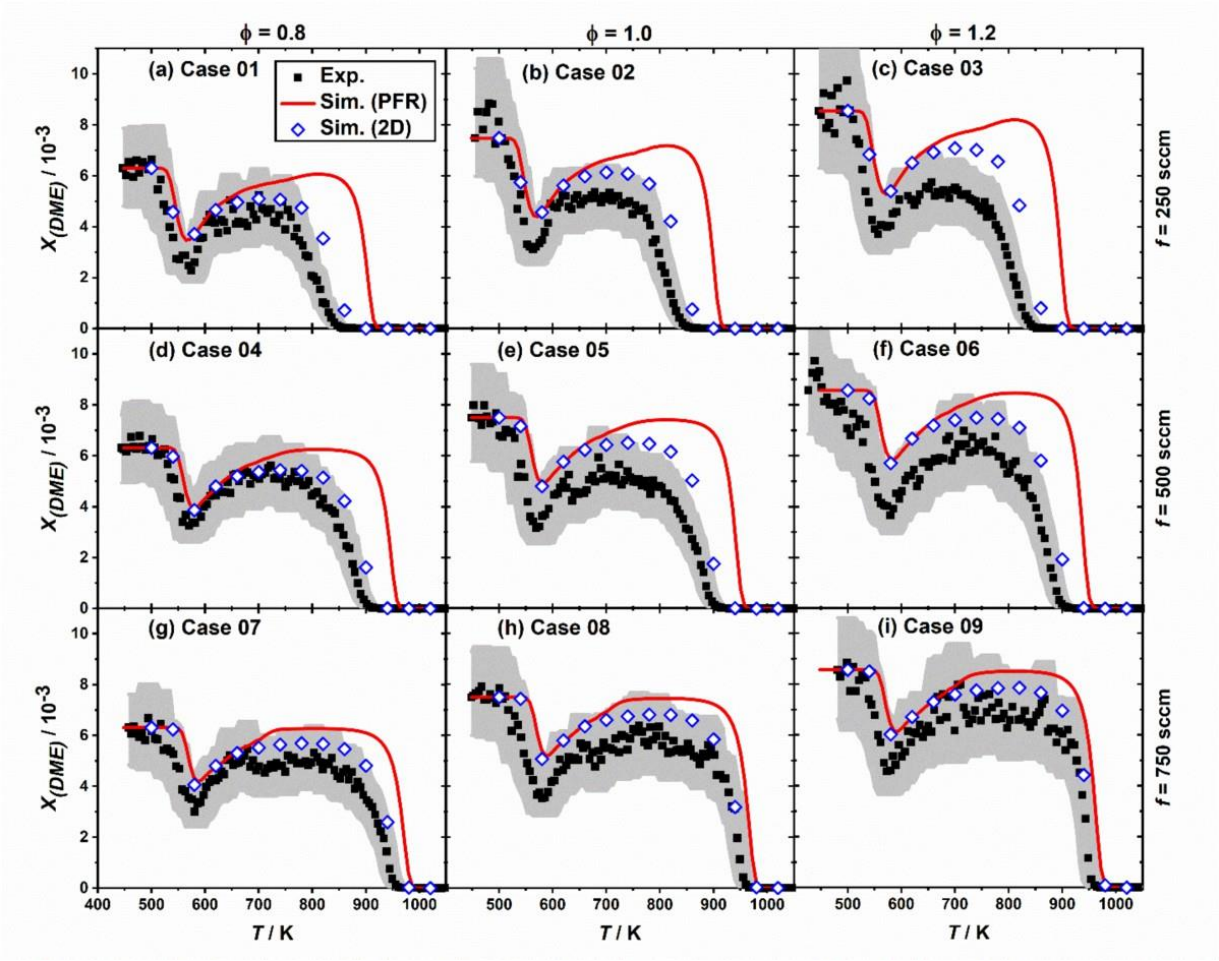

Figure 3: Comparison of measured (black squares) and simulated (red line: PFR, empty blue rhombs: 2D) mole fractions of DME. The experimental uncertainty is indicated by grey shaded areas according to the discussion in Section 2.1 and Table S2 in SM1.

Figure 3 also shows the predicted DME profiles calculated using the PFR assumption and 2D simulations. For the 2D case, mole fraction data were extracted over the reactor axis, after it was properly verified that the species' radial gradients at the reactor exit were not significant in all the conditions (see Fig. 7). The results of PFR and 2D simulations almost coincide at low temperatures, while a significant deviation is obvious in the NTC region and especially at high temperatures. Assuming PFR conditions (*i.e.*, negligible axial diffusion and a flat velocity profile) results in the underestimation of DME reactivity in the NTC region and in a large delay in the predicted onset of high-temperature oxidation. The error introduced adopting the PFR model ranges between ≈25 K and ≈75 K at the short and at the long residence time, respectively.

Both models predict the slight sensitivity of the low-temperature oxidation mechanism to the operating conditions, and the large effect of the residence time on the onset of high-temperature oxidation. However, this effect is only qualitatively predicted when the PFR assumption is adopted, while the agreement is quantitative for the 2D simulations. The predictions of the 2D model are in fact mostly within the uncertainty bands or are outside but very close to the upper boundary.

Figure 4 shows the effect of residence time on the measured and predicted methane profiles exemplarily at lean conditions. Note that profiles of the detected species for all cases are presented in Section S.III. in SM1. Methane is formed through H-abstraction of methyl radicals formed during the high-temperature oxidation pathways of DME presented in Fig. 1. It is evident that the PFR predictions are also delayed here because of the late onset of the high-temperature mechanism. With the 2D simulation, the profile shape is in significantly better agreement with the experimental results, and most of the horizontal shift is actually recovered. The predicted maximum methane mole fraction is within the experimental uncertainty band. However, predictions are close to the lower boundary of the uncertainty region, indicating that the model might need revisions, but new data with smaller uncertainty are needed to constrain the model, because this deviation is not systematic in comparison with other experimental data. This point will be discussed in more detail in Section 4.2.

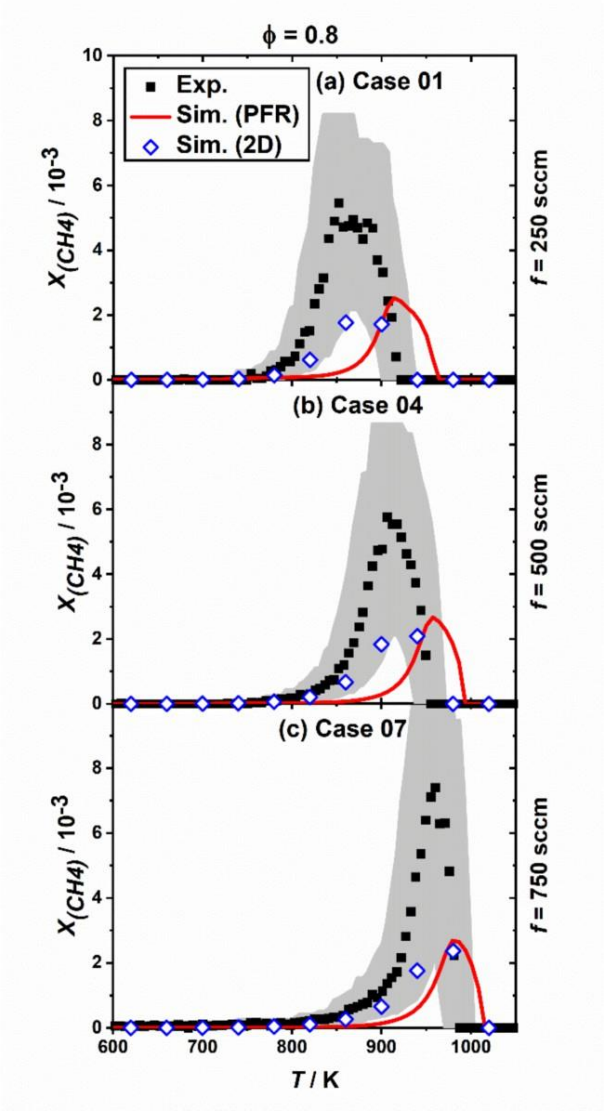

Figure 4: Comparison of measured (black squares) and simulated (red line: PFR, empty blue rhombs: 2D) mole fractions of CH_4 for ϕ=0.8 and all investigated flow rates (250, 500, 750 sccm). The experimental uncertainty is indicated by grey shaded areas according to the discussion in Section 2.1 and Table S2 in SM1.

Figure 5 shows the effect of equivalence ratio on the measured and predicted formaldehyde profiles. The comparison refers to the long residence time. We already noticed that the effect of residence time is important for the high-temperature oxidation and is almost negligible at low temperatures. According to the reaction path diagram in Fig. 1, CH_2O is formed (directly and/or indirectly via CH_3O) during DME oxidation through all the different mechanisms representing the chemistry at low, intermediate (NTC) and high temperatures. Thus, the characteristic double peak of CH_2O observed in Fig. 5 is directly due to the enhanced oxidation of DME at low- and high-temperature conditions. Conversely, the reduced conversion of DME in the NTC region explains the plateau region of CH_2O in the intermediate-temperature range.

Again, in this case, the predictions of the 2D model are within the experimental uncertainty region at all investigated conditions.

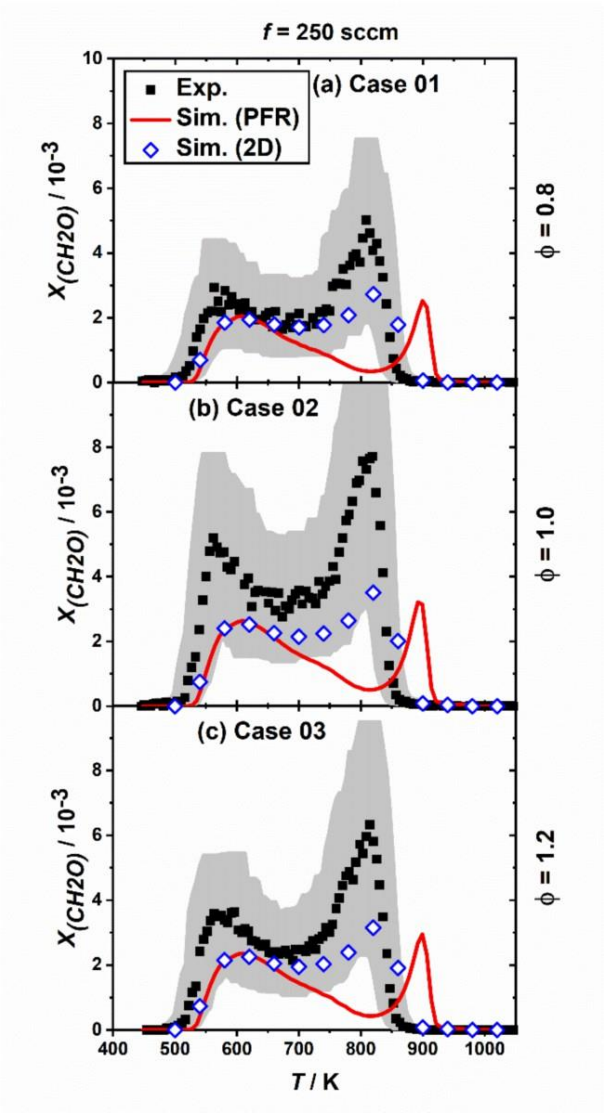

Figure 5: Comparison of measured (black squares) and simulated (red line: PFR, empty blue rhombs: 2D) mole fractions of CH_2O for a total flow rate of 250 sccm and all investigated equivalence ratios (0.8, 1.0, 1.2). The experimental uncertainty is indicated by grey shaded areas according to the discussion in Section 2.1 and Table S2 in SM1.

The comparison of the formaldehyde profiles predicted using the PFR assumption and the 2D model allow to further highlight the systematic errors associated with the PFR model under the present conditions: a negligible deviation to the experiment is seen at low temperatures, while a very large discrepancy is present in the NTC and high-temperature regions. The low conversion of DME in the NTC region and the delayed conversion of DME at high temperatures directly explain these errors in the CH_2O predictions obtained assuming PFR conditions.

To gain a systematical insight on the global reactivity by a quantitative overview of differences between experiments and simulations, temperatures corresponding to 50% fuel conversion T_{50} are shown in Fig. 6 for all investigated conditions. In agreement with the DME mole fraction profiles (see Fig. 3), the discrepancy between experiment and PFR simulations increases with decreasing total flow rates. A similar trend is found for the 2D simulations with a significantly better agreement, though. Therefore, effects of fluid dynamics seem to be most important in the cases 01 to 03 at a total flow rate of 250 sccm corresponding to long residence times. This investigation requires to consider properties in the radial direction, which will be discussed in the following.

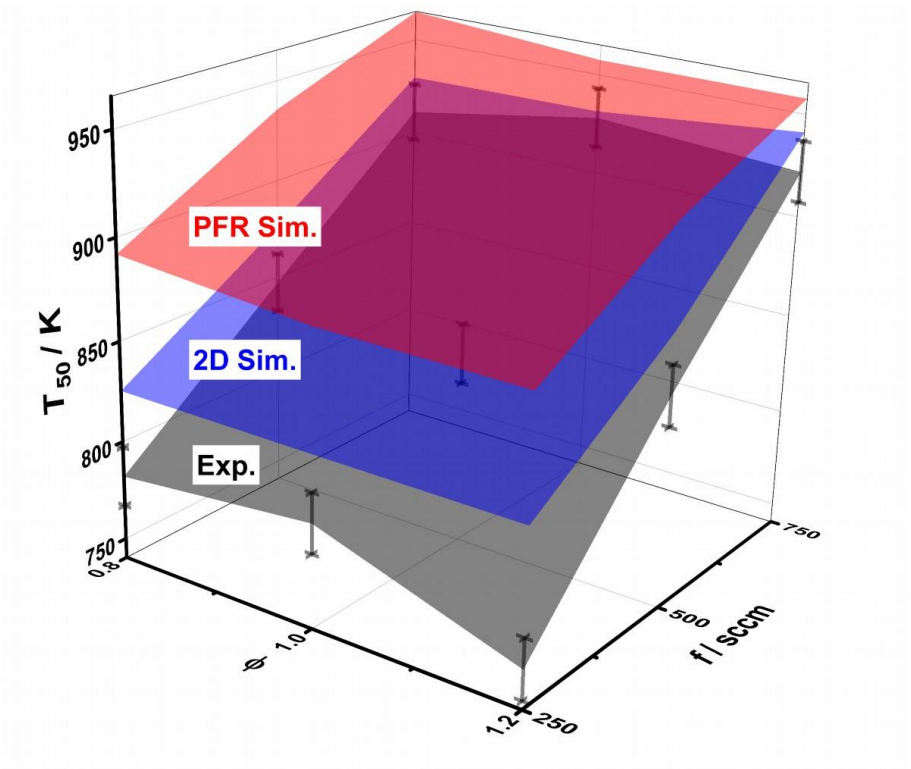

Figure 6: Comparison of measured (grey surface) and simulated (red: PFR, blue: 2D) temperatures corresponding to 50% fuel consumption (T_{50}) in dependence of equivalence ratio ϕ and total flow rate f. An estimated experimental temperature uncertainty of ΔT=±15 K is indicated by error bars.

2D simulations show that the reactor exhibits significant temperature gradients in the radial direction, up to 100 K. To discuss their effects, we refer to case 01 (*i.e.*, flow rate of 250 sccm, ϕ=0.8) at a nominal temperature of 820 K. These temperature gradients are particularly important close to the reactor inlet (Fig. 7), in the region where the temperature is increasing to reach its nominal value at about 10 cm (Fig. S2 in SM1).

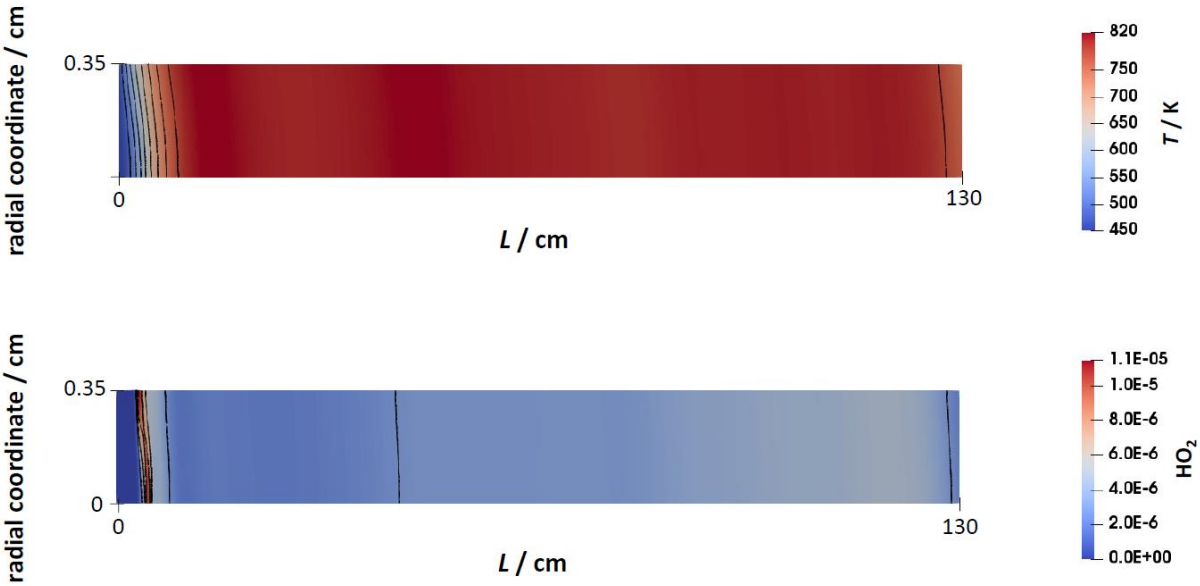

Figure 7: 2D simulation results for case 01 at 820 K: top: 2D temperature map, bottom: 2D HO_2 mass fraction map. For the sake of clarity, the radial coordinate is scaled by a factor 50.

Moreover, the radial profile of the axial velocity is almost parabolic in laminar conditions (*i.e.*, fully developed), and its values vary from zero in the vicinity of the wall up to twice the average velocity on the axis. This difference in the axial velocity has an impact on the residence time, which, of course, increases moving towards the wall. This nearly ideal PFR shows the typical bell-shape curve of the residence time distribution, which we can assume to be a Gaussian function with an average value of 3.95 s and a standard deviation of 0.29 s. This means that ≈15% of the fluid experiences a residence time larger than 4.3 s. Because of the relatively low temperatures, this longer residence time allows for larger reactivity: such an effect cannot be accounted for by assuming a plug-flow model.

The parallel analysis of temperature and residence time allows to understand the larger reactivity predicted by adopting a proper 2D model, in line with the experimental data. A good tracer to explain the radial effects in these conditions is the HO_2 radical. Indeed, HO_2 is one of the most important radicals in controlling the reactivity in the low- and intermediate-temperature range [75], thus it can be considered as a tracer of the chemical evolution in such conditions. Figure 7 (bottom) shows the HO_2 mass fraction along the reactor.

As already said, the temperature gradients and the long residence times close to the wall result in a radial distribution of HO_2 in the very first part of the reactor. On the contrary, the PFR model predicts a negligible amount of HO_2 in the same region, with a mole fraction between 10^{-9} and 10^{-12}, since the low temperature chemistry was not triggered in these conditions. Figure 8 allows to explain this behavior on the basis of

the temperature and HO_2 radial profile at 3, 4 and 5 cm from the inlet. Due to the very low values (10^{-12} – 10^{-9}), HO_2 mole fractions obtained via the PFR model were omitted from Figure 8.

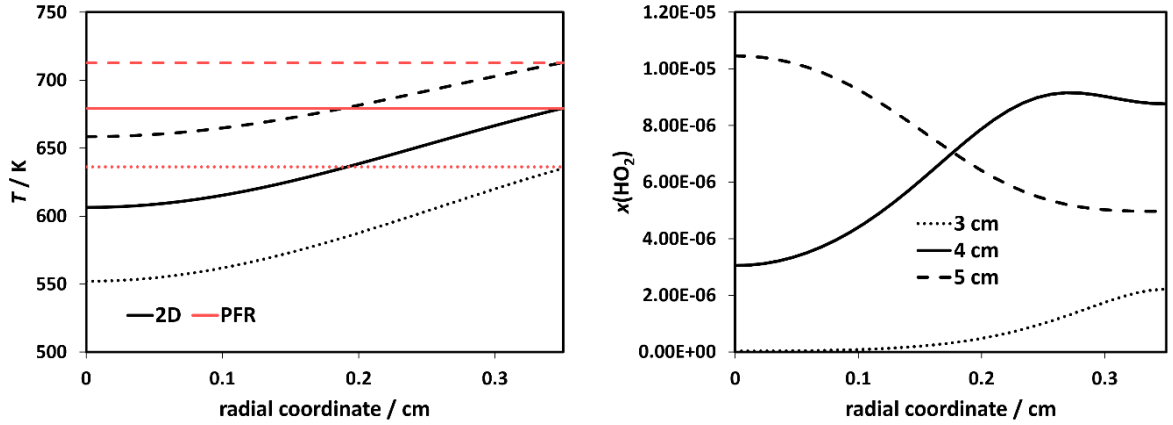

Figure 8: Radial profiles of temperature (left) and HO_2 (right) at different axial distances from inlet.

At 3 cm, the wall temperature is ≈640 K and decreases to ≈550 K on the axis. As it can be seen from Fig. 3, a temperature of 550 K corresponds to low-temperature conditions where the reactivity has not yet reached its maximum, whilst 640 K is already beyond the maximum of the low-temperature conversion in the NTC region. The DME conversion at these temperatures is very similar, but the longer residence time at the wall allows for HO_2 formation, which is negligible on the axis. The low velocity close to the wall is then the origin of the increased reactivity predicted by the 2D model.

At 5 cm, HO_2 is mainly formed in the core of the reactor. In this case, the temperature gradient effect prevails over that of the residence time. The wall temperature of ≈710 K is closer to the minimum reactivity of the NTC region, while the lower axial temperature (≈660 K) entails a larger reactivity, with a net effect of higher HO_2 concentration on the axis.

At 4 cm from the inlet, temperature and residence time compete with each other: the lower temperature favors higher reactivity on the axis, while the residence time increases the reactivity on the wall. This competition results in the presence of a small maximum at about 2.5 mm, with a significant amount of HO_2 in the whole section.

4.2. Kinetic analysis, uncertainties and possible improvements

In addition to the investigation of fluid dynamic effects and their interactions with chemical kinetics found to be largely responsible of the observed deviations at high temperatures in this work, the kinetic model

was carefully analyzed seeking for possibilities of improving its performance by taking advantage of possible remaining uncertainties in the kinetic parameters. A recent study by Bertolino et al. [76] provided a systematic approach to assess rate constants uncertainties. These guidelines were used hereafter selecting the most impactful reactions based on rate of production and sensitivity analyses. To focus on the conditions where the largest deviations were observed, *i.e.*, the onset of high-temperature reactivity, these analyses were performed in an ideal isothermal plug-flow reactor at p=1 atm, τ=2.0 s and T=857 K. Table 4 shows the most sensitive reactions for DME conversion as well as for the formation of the main products methane and formaldehyde whose profiles are directly influenced by the delayed conversion (compare Figs. 3–5). A positive sign stands for a reaction enhancing the formation, or inhibiting the consumption, of a given species and vice versa. The last column of Table 4 reports the estimated uncertainty factor together with the extent of modification needed for improved model performances, *i.e.*, the required action.

Table 4: Top influential reactions for DME oxidation in a plug-flow reactor at T=857 K, τ=2.0 s and p=1 atm. A positive sign stands for a reaction enhancing the formation of the target species and vice versa. The last columns on the right report the estimated uncertainty factor and the required action to improve the model performance: ↑ denotes a rate constant that should be increased, ↓ denotes a rate constant that should be decreased.

	Reaction	Target species and sign (+,-) of sensitivity coefficient			Uncertainty factor	Action
		DME	**CH_4**	**CH_2O**		
R1	$CH_3OCH_3+CH_3 \leftrightarrow CH_4+CH_3OCH_2$	-	+	+	≈3	↑
R2	$CH_3OCH_2 \leftrightarrow CH_2O+CH_3$	+	-	-	≈3	↓
R3	$CH_3OCH_3+HO_2 \leftrightarrow H_2O_2+CH_3OCH_2$	-	+	+	≈3	↑*
R4	$O_2+CH_3OCH_2 \leftrightarrow$ DME-OO	-	+	+	≈5	↑
R5	$O_2+CH_3OCH_2 \rightarrow CH_2O+CH_2O+OH$	-	+	+	≈5	↑
R6	$CH_3OCH_3(+M) \leftrightarrow CH_3O+CH_3(+M)$	-	+	+	≈2	↑
R7	$CH_3OCH_3+O_2 \leftrightarrow HO_2+CH_3OCH_2$	-	+	+	≈3	↑
R8	DME-OO $\rightarrow CH_2O+CH_2O+OH$	-	-	+	≈5	↑
R9	$CH_3OCH_3+CH_3O_2 \leftrightarrow CH_3O_2H+CH_3OCH_2$	-	+	+	≈5	↑

*Notes: * factor of 2 already used in current model version as discussed in Section 3.1.*

Figure 9 shows the effect of the modification of single rate coefficients for the most influential reactions outlined in Table 4. Correction factors that have been applied correspond to those reported as uncertainty

factors in Table 4. Modification of the H-abstraction by methyl radical (R1) is the most effective in increasing DME conversion in the NTC region and at high temperatures, leaving the low-temperature reactivity unchanged. Modification of R2, *i.e.*, decreasing the rate of decomposition of the fuel radical, has a similar positive effect as it enhances the chemically activated pathway (R5) that produces reactive OH radical and increases high-temperature conversion. However, it delays the low-temperature reactivity by ≈40–50 K and decreases the maximum conversion at low temperatures. Further increasing the rate coefficient of H-abstraction by HO_2 by a factor of 1.5 (R3) does not lead to additional improvements compared to the increase of a factor of ≈2 already implemented in the kinetic model. Increasing the rate coefficient of the first O_2 addition reaction (R4) also delays the low-temperature reactivity without improving that at high temperature. The reason is the enhanced stabilization of DME-OO, and with its increased concentration, it inhibits the low-temperature branching channel as the side decomposition to formaldehyde molecules and OH (see Fig. 1), or the backward dissociation becomes favored. This is confirmed by the fact that augmenting the rate coefficient of the chemically activated pathway (R5) decreases the low-temperature conversion (*i.e.*, it inhibits the low-temperature branching pathway) and increases the conversion at high temperature providing highly reactive OH. No significant effects are observed from modifications to reactions (R6) and (R7). This is justified by the fact that the temperature is too low for the unimolecular initiation reaction to be effective in terms of reactive flux. Similarly, the consumption of O_2 largely occurs through the chemically activated pathway (R5) or through the first addition (R4), rather than *via* H-abstraction. Enhancing the reactive flux through (R8) decreases the low-temperature conversion as it inhibits the pathway to the low-temperature branching by forcing DME- OO to propagate the radical chain forming two formaldehyde molecules and OH. No effects are observed at high temperature as the chemically activated pathway (R5) dominates over the first addition to O_2. Increasing the H-abstraction by methyl peroxy radical (CH_3O_2) on DME increases the conversion in the NTC region, without influencing the low- and high-temperature reactivity.

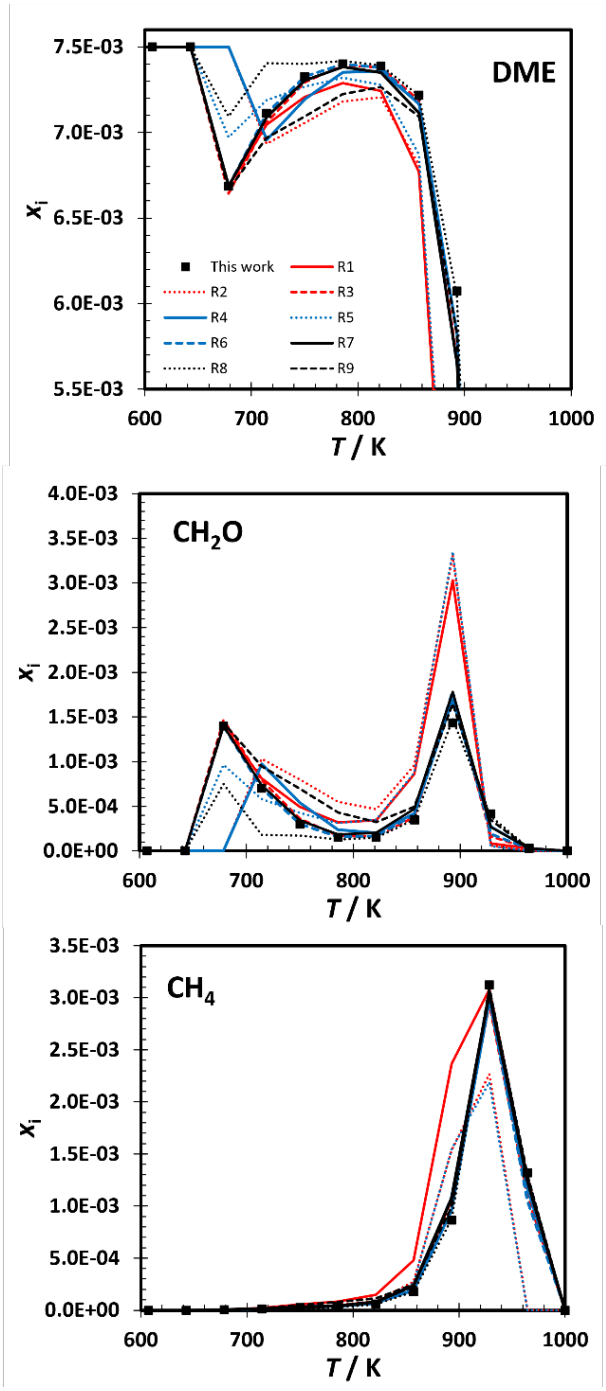

Figure 9: Effect of modification of the most influential rate coefficients reported in Table 4 on DME conversion as well as methane (CH_4) and formaldehyde (CH_2O) profiles. Plug-flow reactor simulations were performed at 0.75% DME-O_2/Ar, ϕ=1.0, p=1 atm, τ=2 s.

Results from the same analysis on the ignition delay times of DME/air mixtures at p=10 atm and T=650–1250 K are reported in Section S.IV. of SM1. In this case the most significant effects are given by (R2) and (R8) and are limited to the NTC region. Decreasing (R2) promotes the low-temperature branching pathway thus shortening the ignition delay times by up to a factor higher than 2. Conversely, increasing the

decomposition of DME-OO (R8) decreases the ignition propensity by a factor higher than 2. Rate of production and sensitivity analysis results at *T*=685 K and *T*=857 K for flow reactor simulations are also reported in Section S.IV. of SM1.

4.3 A wide-range benchmarking *via* Curve Matching

In order to quantify and visualize the performance of the kinetic model in predicting the formation and consumption of the measured species, the numerical framework introduced by Bernardi et al. [77] and further improved by Pelucchi et al. [78], known as Curve Matching, was adopted. This approach is based on the functional analysis of the values determined from experiments and models, obtained *via* interpolating, smoothed splines. The Curve Matching approach can thus compare numerous sets of discrete experimental data with the numerical results of different model predictions in a quantitative fashion. The accuracy of the predictions obtained *via* both PFR and 2D approaches (see Figs. 3–5) by using the developed mechanism was quantified through the characterizing indices resulting from such a framework. It is worth reminding that '1' indicates perfect agreement between them, while '0' indicates the maximum dissimilarity. For the sake of comprehensiveness, other literature mechanisms [20,25,39,43,50,79,80] were included by using the PFR model, too. Results are shown under the form of a heat map in Fig. 10. Considering the PFR model, it can be noticed that the CRECK and the Wang mechanisms behave slightly better than the others, whose indices worsen especially for the lowest flow rates (cases 01–03). However, as also previously observed (although in a qualitative fashion), the most significant improvements are obtained by changing the reactor model, rather than the mechanism. Especially at 250 sccm and 500 sccm (cases 01–06), the indices affecting the major species are significantly improved when using the 2D modeling approach. An exception is represented by CO_2, whose indices are much worse than the PFR case. However, this is attributable to the peculiarity of the CO_2 profile (see Fig. S5 in SM1) that has a steep increase at the onset temperature, compared to the other measured species, exhibiting a smoother profile. The lower amount of 2D simulations (*i.e.*, one solution every 40 K), due to the higher computing requirements, results then in an insufficient refinement of the CO_2 profile, such that the interpolating splines cannot reproduce the steep increase in the onset region.

Figure 10: Heat map resulting from Curve Matching indices, for assessing the performance of different mechanisms in reproducing experimental data through the PFR model. Literature mechanisms from Burke et al. [20], Zhao et al. [25], Reuter et al. [39]: "HPMech v3.3", Wang et al. [43], Shreshtha et al. [50], Zhou et al. [79]: "Aramco 3.0", Hashemi et al. [80]: "DTU".

5 Summary and conclusion

In the context of the increasing importance of alternative transportation fuels that could be sustainably produced and offer a potential of reduced local emissions, this study has aimed at an analysis of the uncertainties from experiment and modeling approaches for one of the chemically simplest fuel molecules in this respect, dimethyl ether, which can also be regarded as the smallest member of the OME family. The knowledge about such uncertainties, not only for the case of DME, is of interest for the reliable simulation

of combustion processes. When using kinetic mechanisms to represent the oxidation chemistry of such fuels, potentially also in hydrogen-rich or other blends or in conditions relevant to combustion as well as aftertreatment environments, one must rely on a realistic performance assessment of the model over an extended temperature (and pressure) range. Obviously, a systematically constructed mechanism should be tested to include the most reliable reaction set for each individual fuel compound. The case of DME has appeared as particularly interesting for the present investigation not only because of its attractive characteristics as an alternative fuel, but also because of the wealth of existing experimental and modeling information with validation efforts in many environments suitable to analyze detailed chemistry, including shock tubes, rapid compression machines, jet-stirred and plug-flow reactors and different flame configurations. Detailed insight on low- and high-temperature oxidation mechanisms is thus available. A plug-flow reactor was selected here as the target because speciation analysis along the reaction coordinate is possible in this configuration separating reactants and products, and because the interplay of reaction kinetics and fluid dynamics can be studied.

Specifically, we have used electron ionization mass spectrometry coupled to a given PFR to provide quantitative species profiles as a function of temperature in the range of 400–1100 K at near-atmospheric pressure (970 mbar) over a wide range of conditions. Nine cases were selected with three different equivalence ratios ϕ (0.8, 1.0 and 1.2) and three different flow rates f at each condition (250 sccm, 500 sccm and 750 sccm), representing a range of residence times τ of 1.1 to 6.9 s, to study DME oxidation and influences of fluid dynamics systematically. All conditions were first simulated using a PFR model with the CRECK mechanism, which was systematically analyzed and updated. To this end, existing recent mechanisms and reaction kinetic data were examined, and replacements and additions to the starting version of the mechanism were performed when deemed necessary. A comparison of the experimental data, the species-specific uncertainties of which were carefully assessed, with this updated mechanism showed appreciable agreement over all cases in the low-temperature regime, including the simulation results for key intermediates such as methane and formaldehyde. Significant deviations between the experiment and PFR model results were seen in the temperature range beyond the NTC region, near and above 700 K, where the fuel conversion was noticeably slower than in the experiment. These deviations were most prominent for the cases with lower flow rates, *i.e.*, larger residence times, and only marginally depending on the stoichiometry.

This behavior motivated us to assume fluid dynamics influences particularly at those conditions and consequentially, to perform simulations with a two-dimensional CFD approach. The results showed surprisingly good agreement within experimental uncertainty for all nine cases and species measured,

proving that such 2D influences could not be neglected under these conditions. Radial profiles of temperature and species at the conditions with low flow rates highlight the noted effect in terms of the radial temperature distribution and the temperature-sensitive reactions occurring close to the inlet. A further result of this analysis is the importance of conditions, or better of chemistry, on fluid dynamics. The reactor behaves as a PFR in low-temperature conditions, *i.e.*, at temperatures lower than about 650 K, whilst the ideality fails and radial effects become important at higher temperatures. In a wider perspective, such an outcome can be useful to understand previous experimental data, with different setups and fuels, that could not be described adequately even with state-of-the-art mechanisms.

To examine whether similar or further improvements could have resulted from additional modifications of the chemical reaction mechanism, the most influential reactions affecting DME conversion were identified and tentatively modified to analyze the resulting effects. The subsequent changes seen in the species profiles upon these modifications, occurring in different temperature regimes, could all be reconciled with the general understanding of the DME oxidation chemistry, but none of the modifications provided good agreement with the experimental data. A rate of production and sensitivity analysis was performed at two selected temperatures, 685 K and 857 K, corresponding to a region below and within the deviations noted with the PFR model. Different reactions of the low-, intermediate- and high-temperature chemistry are predominant at these temperatures.

In this context, it is interesting to note that the origin of some of the intermediates detected in different DME oxidation studies remains somewhat unclear. Also, reactions in the H_2 and C_1 subsets have not been analyzed in their entirety with most recent methods of theory. Reactions deserving further investigation at the lower temperature (near 685 K) include the second addition to O_2 and pathways to acid formation, whereas at the higher temperature (near 857 K), reactions in the methane, formaldehyde and hydrogen subset are among those sensitive ones that may need further inspection.

As a final benchmarking attempt, several recent mechanisms were examined using the PFR model against the experimental data by means of a curve matching procedure. The results, presented in terms of a heat map, demonstrate clearly that the best agreement of the simulation with the experiments is obtained with the 2D CFD modeling approach, underlining that the interplay of reaction kinetics and fluid dynamics is a key factor under the investigated conditions, especially at lower flow rates or longer residence times.

It is suggested that potential discrepancies noted between experimental data and modeling results should always consider the associated uncertainties at both ends, using preferably also a realistic representation in figures to avoid misleading interpretations of agreement. Furthermore, updating mechanisms with

improved rate coefficients and added reactions should be done with care to understand and reflect the changes made with their consequences for the general reaction pathways, and not just with the aim to obtain a better appearance or fit for the case in question. Finally, further investigation about radial effects in laminar flow are needed, beyond the results reported in this work. Together with Bodenstein number and vessel geometry, already discussed by Levenspiel [71], fuel and its reactivity play a role in the choice of the proper model of the flow reactors. Although it is significantly more computationally costly, some experimental cases may merit an inspection with a higher-dimensional CFD simulation to check for influences of fluid dynamics rather than focusing on the reaction chemistry alone.

Acknowledgements

This work was in part supported by the Deutsche Forschungsgemeinschaft (DFG) in project KO 1363/34-1 which is gratefully acknowledged.

Credit author statement

AS: PFR and 2D simulations, Formal Analysis, Writing - Original draft preparation

SS: Experimental investigations, Visualization, Writing - Original draft preparation

MP: Model development and analysis, Writing - Original draft preparation

AF: Literature review, Writing - Original draft preparation

KKH: Conceptualization, Supervision, Project administration, Writing - Review and editing

TF: Conceptualization, Supervision, Project administration, Writing - Review and editing

References

[1] Sustainable Development Goals, United Nations Department of Economic and Social Affairs, https://sdgs.un.org/goals, accessed: 03/21/2021.

[2] D.P. van Vuuren, E. Stehfest, D.E.H.J. Gernaat, M. van den Berg, D.L. Bijl, H.S. de Boer, V. Daioglou, J.C. Doelman, O.Y. Edelenbosch, M. Harmsen, A.F. Hof, M.A.E. van Sluisveld, Alternative pathways to the 1.5 °C target reduce the need for negative emission technologies, Nat. Clim. Chang. 8 (2018) 391–397.

[3] A. Buttler, H. Spliethoff, Current status of water electrolysis for energy storage, grid balancing and sector coupling via power-to-gas and power-to-liquids: A review, Renew. Sustain. Energy Rev. 82 (2018) 2440–2454.

[4] BP Energy Outlook 2020, https://safety4sea.com/wp-content/uploads/2020/09/BP-Energy-Outlook-2020-2020_09.pdf, accessed: 03/21/2021

[5] S. Schemme, J.L. Breuer, M. Köller, S. Meschede, F. Walman, R.C. Samsun, R. Peters, D. Stolten, H2-based synthetic fuels: A techno-economic comparison of alcohol, ether and hydrocarbon production, Int. J. Hydrogen Energy 45 (2020) 5395–5414.

[6] A. König, K. Ulonska, A. Mitsos, J. Viell, Optimal Applications and Combinations of Renewable Fuel Production from Biomass and Electricity, Energy Fuels 33 (2019) 1659–1672.

[7] L.S. Tran, B. Sirjean, P.A. Glaude, R. Fournet, F. Battin-Leclerc, Progress in detailed kinetic modeling of the combustion of oxygenated components of biofuels, Energy 43 (2012) 4–18.

[8] S.M. Sarathy, P. Oßwald, N. Hansen, K. Kohse-Höinghaus, Alcohol combustion chemistry, Prog. Energy Combust. Sci. 44 (2014) 40–102.

[9] W. Leitner, J. Klankermayer, S. Pischinger, H. Pitsch, K. Kohse-Höinghaus, Advanced Biofuels and Beyond: Chemistry Solutions for Propulsion and Production, Angew. Chemie Int. Ed. 56 (2017) 5412–5452.

[10] M.A. Eldeeb, B. Akih-Kumgeh, Recent Trends in the Production, Combustion and Modeling of Furan-Based Fuels, Energies 11 (2018) 512.

[11] B. Heuser, P. Mauermann, R. Wankhade, F. Kremer, S. Pischinger, Combustion and emission behavior of linear C_8-oxygenates, Int. J. Engine Res. 16 (2015) 627–638.

[12] A. Omari, B. Heuser, S. Pischinger, C. Rüdinger, Potential of long-chain oxymethylene ether and oxymethylene ether-diesel blends for ultra-low emission engines, Appl. Energy 239 (2019) 1242–1249.

[13] S. Deutz, D. Bongartz, B. Heuser, A. Kätelhön, L. Schulze Langenhorst, A. Omari, M. Walters, J. Klankermayer, W. Leitner, A. Mitsos, S. Pischinger, A. Bardow, Cleaner production of cleaner fuels: wind-to-wheel – environmental assessment of CO_2-based oxymethylene ether as a drop-in fuel, Energy Environ. Sci. 11 (2018) 331–343.

[14] P. Bokinge, S. Heyne, S. Harvey, Renewable OME from biomass and electricity—Evaluating carbon footprint and energy performance, Energy Sci. Eng. 8 (2020) 2587–2598.

[15] S. Eckart, L. Cai, C. Fritsche, F. vom Lehn, H. Pitsch, H. Krause, Laminar burning velocities, CO, and NOx emissions of premixed polyoxymethylene dimethyl ether flames, Fuel 293 (2021) 120321.

[16] L. Cai, S. Jacobs, R. Langer, F. vom Lehn, K.A. Heufer, H. Pitsch, Auto-ignition of oxymethylene ethers (OME_n, n = 2–4) as promising synthetic e-fuels from renewable electricity: shock tube experiments and automatic mechanism generation, Fuel 264 (2020) 116711.

[17] K. Moshammer, A.W. Jasper, D.M. Popolan-Vaida, A. Lucassen, P. Diévart, H. Selim, A.J. Eskola, C.A. Taatjes, S.R. Leone, S.M. Sarathy, Y. Ju, P. Dagaut, K. Kohse-Höinghaus, N. Hansen, Detection and Identification of the Keto-Hydroperoxide ($HOOCH_2OCHO$) and Other Intermediates during Low-Temperature Oxidation of Dimethyl Ether, J. Phys. Chem. A 119 (2015) 7361–7374.

[18] J. De Vries, W.B. Lowry, Z. Serinyel, H.J. Curran, E.L. Petersen, Laminar flame speed measurements of dimethyl ether in air at pressures up to 10 atm, Fuel 90 (2011) 331–338.

[19] H. Hashemi, J.M. Christensen, P. Glarborg, High-pressure pyrolysis and oxidation of DME and DME/CH_4, Combust. Flame 205 (2019) 80–92.

[20] U. Burke, K.P. Somers, P. O'Toole, C.M. Zinner, N. Marquet, G. Bourque, E.L. Petersen, W.K. Metcalfe, Z. Serinyel, H.J. Curran, An ignition delay and kinetic modeling study of methane, dimethyl ether, and their mixtures at high pressures, Combust. Flame 162 (2015) 315–330.

[21] G. Mittal, M. Chaos, C.J. Sung, F.L. Dryer, Dimethyl ether autoignition in a rapid compression machine: Experiments and chemical kinetic modeling, Fuel Process. Technol. 89 (2008) 1244–1254.

[22] Z. Shi, H. Zhang, H. Lu, H. Liu, Y. A, F. Meng, Autoignition of DME/H_2 mixtures in a rapid compression machine under low-to-medium temperature ranges, Fuel 194 (2017) 50–62.

[23] U. Pfahl, K. Fieweger, G. Adomeit, Self-ignition of diesel-relevant hydrocarbon-air mixtures under engine conditions, Symp. (Int.) Combust. 26 (1996) 781–789.

[24] X. Qin, Y. Ju, Measurements of burning velocities of dimethyl ether and air premixed flames at elevated pressures, Proc. Combust. Inst. 30 (2005) 233–240.

[25] Z. Zhao, M. Chaos, A. Kazakov, F.L. Dryer, Thermal decomposition reaction and a comprehensive kinetic model of dimethyl ether, Int. J. Chem. Kinet. 40 (2008) 1–18.

[26] P. Dagaut, J.C. Boettner, M. Cathonnet, Chemical kinetic study of dimethylether oxidation in a jet stirred reactor from 1 to 10 ATM: Experiments and kinetic modeling, Symp. (Int.) Combust. 26 (1996) 627–632.

[27] P. Dagaut, C. Daly, J.M. Simmie, M. Cathonnet, The oxidation and ignition of dimethylether from low to high temperature (500-1600 K): Experiments and kinetic modeling, Symp. (Int.)

Combust. 27 (1998) 361–369.

[28] N.L. Le Tan, M. Djehiche, C.D. Jain, P. Dagaut, G. Dayma, Quantification of HO_2 and other products of dimethyl ether oxidation (H_2O_2, H_2O, and CH_2O) in a jet-stirred reactor at elevated temperatures by low-pressure sampling and continuous-wave cavity ring-down spectroscopy, Fuel 158 (2015) 248–252.

[29] A. Rodriguez, O. Frottier, O. Herbinet, R. Fournet, R. Bounaceur, C. Fittschen, F. Battin-Leclerc, Experimental and Modeling Investigation of the Low-Temperature Oxidation of Dimethyl Ether, J. Phys. Chem. A 119 (2015) 7905–7923.

[30] K. Moshammer, A.W. Jasper, D.M. Popolan-Vaida, Z. Wang, V.S. Bhavani Shankar, L. Ruwe, C.A. Taatjes, P. Dagaut, N. Hansen, Quantification of the Keto-Hydroperoxide ($HOOCH_2OCHO$) and Other Elusive Intermediates during Low-Temperature Oxidation of Dimethyl Ether, J. Phys. Chem. A 120 (2016) 7890–7901.

[31] M.U. Alzueta, J. Muro, R. Bilbao, P. Glarborg, Oxidation of Dimethyl Ether and its Interaction with Nitrogen Oxides, Isr. J. Chem. 39 (1999) 73–86.

[32] A. Schönborn, P. Sayad, A.A. Konnov, J. Klingmann, Autoignition of Dimethyl Ether and Air in an Optical Flow-Reactor, Energy Fuels 28 (2014) 4130–4138.

[33] H.J. Curran, S.L. Fischer, F.L. Dryer, Reaction kinetics of dimethyl ether. II: low-temperature oxidation in flow reactors, Int. J. Chem. Kinet. 32 (2000) 741–759.

[34] L. Marrodán, Á.J. Arnal, Á. Millera, R. Bilbao, M.U. Alzueta, The inhibiting effect of NO addition on dimethyl ether high-pressure oxidation, Combust. Flame 197 (2018) 1–10.

[35] D. Kaczmarek, J. Herzler, S. Porras, S. Shaqiri, M. Fikri, C. Schulz, B. Atakan, U. Maas, T. Kasper, Plug-flow reactor and shock-tube study of the oxidation of very fuel-rich natural gas/DME/O2 mixtures, Combust. Flame 225 (2021) 86–103.

[36] S. Porras, D. Kaczmarek, J. Herzler, S. Drost, M. Werler, T. Kasper, M. Fikri, R. Schießl, B. Atakan, C. Schulz, U. Maas, An experimental and modeling study on the reactivity of extremely fuel-rich methane/dimethyl ether mixtures, Combust. Flame 212 (2020) 107–122.

[37] X.L. Zheng, T.F. Lu, C.K. Law, C.K. Westbrook, H.J. Curran, Experimental and computational study of nonpremixed ignition of dimethyl ether in counterflow, Proc. Combust. Inst. 30 (2005) 1101–1109.

[38] Y. Jiang, R. Gehmlich, T. Knoblinger, K. Seshadri, Experimental and computational investigation of partially-premixed methoxymethane flames, Combust. Flame 195 (2018) 99–104.

[39] C.B. Reuter, R. Zhang, O.R. Yehia, Y. Rezgui, Y. Ju, Counterflow flame experiments and chemical kinetic modeling of dimethyl ether/methane mixtures, Combust. Flame 196 (2018) 1–10.

[40] H.J. Curran, W.J. Pitz, C.K. Westbrook, P. Dagaut, J.-C. Boettner, M. Cathonnet, A wide

range modeling study of dimethyl ether oxidation, Int. J. Chem. Kinet. 30 (1998) 229–241.

[41] S.L. Fischer, F.L. Dryer, H.J. Curran, The reaction kinetics of dimethyl ether. I: High-temperature pyrolysis and oxidation in flow reactors, Int. J. Chem. Kinet. 32 (2000) 713–740.

[42] E.E. Dames, A.S. Rosen, B.W. Weber, C.W. Gao, C.J. Sung, W.H. Green, A detailed combined experimental and theoretical study on dimethyl ether/propane blended oxidation, Combust. Flame 168 (2016) 310–330.

[43] Z. Wang, X. Zhang, L. Xing, L. Zhang, F. Herrmann, K. Moshammer, F. Qi, K. Kohse-Höinghaus, Experimental and kinetic modeling study of the low- and intermediate-temperature oxidation of dimethyl ether, Combust. Flame 162 (2015) 1113–1125.

[44] P. Glarborg, M.U. Alzueta, K. Dam-Johansen, J.A. Miller, Kinetic Modeling of Hydrocarbon/Nitric Oxide Interactions in a Flow Reactor, Combust. Flame 115 (1998) 1–27.

[45] D. Liu, J. Santner, C. Togbé, D. Felsmann, J. Koppmann, A. Lackner, X. Yang, X. Shen, Y. Ju, K. Kohse-Höinghaus, Flame structure and kinetic studies of carbon dioxide-diluted dimethyl ether flames at reduced and elevated pressures, Combust. Flame 160 (2013) 2654–2668.

[46] F. Herrmann, B. Jochim, P. Oßwald, L. Cai, H. Pitsch, K. Kohse-Höinghaus, Experimental and numerical low-temperature oxidation study of ethanol and dimethyl ether, Combust. Flame 161 (2014) 384–397.

[47] N. Kurimoto, B. Brumfield, X. Yang, T. Wada, P. Diévart, G. Wysocki, Y. Ju, Quantitative measurements of HO_2/H_2O_2 and intermediate species in low and intermediate temperature oxidation of dimethyl ether, Proc. Combust. Inst. 35 (2015) 457–464.

[48] J.C. Prince, F.A. Williams, A short reaction mechanism for the combustion of dimethyl-ether, Combust. Flame 162 (2015) 3589–3595.

[49] A.J. Eskola, S.A. Carr, R.J. Shannon, B. Wang, M.A. Blitz, M.J. Pilling, P.W. Seakins, S.H. Robertson, Analysis of the Kinetics and Yields of OH Radical Production from the CH_3OCH_2 + O_2 Reaction in the Temperature Range 195–650 K: An Experimental and Computational study, J. Phys. Chem. A 118 (2014) 6773–6788.

[50] K.P. Shrestha, S. Eckart, A.M. Elbaz, B.R. Giri, C. Fritsche, L. Seidel, W.L. Roberts, H. Krause, F. Mauss, A comprehensive kinetic model for dimethyl ether and dimethoxymethane oxidation and NO_x interaction utilizing experimental laminar flame speed measurements at elevated pressure and temperature, Combust. Flame 218 (2020) 57–74.

[51] Z. Wang, O. Herbinet, N. Hansen, F. Battin-Leclerc, Exploring hydroperoxides in combustion: History, recent advances and perspectives, Prog. Energy Combust. Sci. 73 (2019) 132–181.

[52] A.S. Tomlin, E. Agbro, V. Nevrlý, J. Dlabka, M. Vašinek, Evaluation of Combustion Mechanisms Using Global Uncertainty and Sensitivity Analyses: A Case Study for Low-Temperature Dimethyl Ether Oxidation, Int. J. Chem. Kinet. 46 (2014) 662–682.

[53] W.K. Metcalfe, S.M. Burke, S.S. Ahmed, H.J. Curran, A hierarchical and comparative kinetic modeling study of C_1 - C_2 hydrocarbon and oxygenated fuels, Int. J. Chem. Kinet. 45 (2013) 638–675.

[54] F.L. Dryer, F.M. Haas, J. Santner, T.I. Farouk, M. Chaos, Interpreting chemical kinetics from complex reaction-advection-diffusion systems: Modeling of flow reactors and related experiments, Prog. Energy Combust. Sci. 44 (2014) 19–39.

[55] T. Wada, A. Sudholt, H. Pitsch, N. Peters, Analysis of first stage ignition delay times of dimethyl ether in a laminar flow reactor, Combust. Theory Model 17 (2013) 906–936.

[56] H. Guo, W. Sun, F.M. Haas, T. Farouk, F.L. Dryer, Y. Ju, Measurements of H2O2 in low temperature dimethyl ether oxidation, Proc. Combust. Inst. 34 (2013) 573–581.

[57] C. Hemken, U. Burke, K.-Y. Lam, D.F. Davidson, R.K. Hanson, K.A. Heufer, K. Kohse-Höinghaus, Toward a better understanding of 2-butanone oxidation: Detailed species measurements and kinetic modeling, Combust. Flame 184 (2017) 195–207.

[58] H. Jin, J. Pieper, C. Hemken, E. Bräuer, L. Ruwe, K. Kohse-Höinghaus, Chemical interaction of dual-fuel mixtures in low-temperature oxidation, comparing n-pentane/dimethyl ether and n-pentane/ethanol, Combust. Flame 193 (2018) 36–53.

[59] S. Schmitt, S. Schwarz, L. Ruwe, J. Horstmann, F. Sabath, L. Maier, O. Deutschmann, K. Kohse-Höinghaus, Homogeneous conversion of NO_x and NH_3 with CH_4 , CO, and C_2H_4 at the diluted conditions of exhaust-gases of lean operated natural gas engines, Int. J. Chem. Kinet. 53 (2021) 213–229.

[60] M. Schenk, L. Leon, K. Moshammer, P. Oßwald, T. Zeuch, L. Seidel, F. Mauss, K. Kohse-Höinghaus, Detailed mass spectrometric and modeling study of isomeric butene flames, Combust. Flame 160 (2013) 487–503.

[61] H. Zhang, S. Schmitt, L. Ruwe, K. Kohse-Höinghaus, Inhibiting and promoting effects of NO on dimethyl ether and dimethoxymethane oxidation in a plug-flow reactor, Combust. Flame 224 (2021) 94–107.

[62] A. Kéromnès, W.K. Metcalfe, K.A. Heufer, N. Donohoe, A.K. Das, C.J. Sung, J. Herzler, C. Naumann, P. Griebel, O. Mathieu, M.C. Krejci, E.L. Petersen, W.J. Pitz, H.J. Curran, An experimental and detailed chemical kinetic modeling study of hydrogen and syngas mixture oxidation at elevated pressures, Combust. Flame 160 (2013) 995-1011.

[63] G. Bagheri, E. Ranzi, M. Pelucchi, A. Parente, A. Frassoldati, T. Faravelli, Comprehensive kinetic study of combustion technologies for low environmental impact: MILD and OXY-fuel combustion of methane, Combust. Flame 212 (2020) 142–155.

[64] E. Ranzi, A. Frassoldati, A. Stagni, M. Pelucchi, A. Cuoci, T. Faravelli, Reduced kinetic schemes of complex reaction systems: Fossil and biomass-derived transportation fuels, Int. J. Chem. Kinet. 46 (2014) 512–542.

[65] A. Jalan, I.M. Alecu, R. Meana-Pañeda, J. Aguilera-Iparraguirre, K.R. Yang, S.S. Merchant, D.G. Truhlar, W.H. Green, New Pathways for Formation of Acids and Carbonyl Products in

Low-Temperature Oxidation: The Korcek Decomposition of γ-Ketohydroperoxides, J. Am. Chem. Soc. 135 (2013) 11100–11114.

[66] E. Ranzi, C. Cavallotti, A. Cuoci, A. Frassoldati, M. Pelucchi, T. Faravelli, New reaction classes in the kinetic modeling of low temperature oxidation of n-alkanes, Combust. Flame 162 (2015) 1679–1691.

[67] C. Cavallotti, M. Pelucchi, A. Frassoldati, Analysis of acetic acid gas phase reactivity: Rate constant estimation and kinetic simulations, Proc. Combust. Inst. 37 (2019) 539–546.

[68] C. Cavallotti, M. Pelucchi, Y. Georgievskii, S.J. Klippenstein, EStokTP: Electronic Structure to Temperature- and Pressure-Dependent Rate Constants—A Code for Automatically Predicting the Thermal Kinetics of Reactions, J. Chem. Theory Comput. 15 (2019) 1122–1145.

[69] E. Ranzi, P. Gaffuri, T. Faravelli, P. Dagaut, A wide-range modeling study of n-heptane oxidation, Combust. Flame 103 (1995) 91–106.

[70] H.J. Curran, P. Gaffuri, W.J. Pitz, C.K. Westbrook, A comprehensive modeling study of n-heptane oxidation, Combust. Flame 114 (1998) 149–177.

[71] O. Levenspiel, Chemical reaction engineering - 3rd ed, John Wiley & Sons, New York (1999).

[72] A. Cuoci, A. Frassoldati, T. Faravelli, E. Ranzi, OpenSMOKE++: An object-oriented framework for the numerical modeling of reactive systems with detailed kinetic mechanisms, Comput. Phys. Commun. 192 (2015) 237–264.

[73] T.P. Coffee, J.M. Heimerl, Transport algorithms for premixed, laminar steady-state flames, Combust. Flame 43 (1981) 273–289.

[74] A. Cuoci, A. Frassoldati, T. Faravelli, E. Ranzi, Numerical Modeling of Laminar Flames with Detailed Kinetics Based on the Operator-Splitting Method, Energy Fuels 27 (2013) 7730–7753.

[75] H.J. Curran, P. Gaffuri, W.J. Pitz, C.K. Westbrook, A comprehensive modeling study of n-heptane oxidation, Combust. Flame 114 (1998) 149–177.

[76] A. Bertolino, M. Fürst, A. Stagni, A. Frassoldati, M. Pelucchi, C. Cavallotti, T. Faravelli, A. Parente, An evolutionary, data-driven approach for mechanism optimization: theory and application to ammonia combustion, Combust. Flame 229 (2021) 111366.

[77] M.S. Bernardi, M. Pelucchi, A. Stagni, L.M. Sangalli, A. Cuoci, A. Frassoldati, P. Secchi, T. Faravelli, Curve matching, a generalized framework for models/experiments comparison: An application to n-heptane combustion kinetic mechanisms, Combust. Flame 168 (2016) 186–203.

[78] M. Pelucchi, A. Stagni, T. Faravelli, Addressing the complexity of combustion kinetics: Data management and automatic model validation, Comput. Aided Chem. Eng., Elsevier B.V., (2019) 763–798.

[79] C.W. Zhou, Y. Li, U. Burke, C. Banyon, K.P. Somers, S. Ding, S. Khan, J.W. Hargis, T. Sikes, O.,

Mathieu, E.L. Petersen, M. AlAbbad, A. Farooq, Y. Pan, Y. Zhang, Z. Huang, J. Lopez, Z. Loparo, S.S. Vasu, H.J. Curran, An experimental and chemical kinetic modeling study of 1,3-butadiene combustion: Ignition delay time and laminar flame speed measurements, Combust. Flame 197 (2018) 423–438.

[80] H. Hashemi, J.M. Christensen, P. Glarborg, High-pressure pyrolysis and oxidation of ethanol, Fuel 218 (2018) 247–257.